Electronic Supplementary Information

Selective CO_2 reduction to C_3 and C_4 oxhydrocarbons on nickel phosphides at overpotentials as low as 10 mV

Karin U. D. Calvinho[a†], Anders B. Laursen[a†], Kyra M. K. Yap[a], Timothy A. Goetjen[a], Shinjae Hwang[a], Nagarajan Murali[a], Bryan Mejia-Sosa[b], Alexander Lubarski[a], Krishani M. Teeluck[a], Eugene S. Hall[a], Eric Garfunkel[a], Martha Greenblatt[a], and G. Charles Dismukes[a,b*]

[a]Department of Chemistry and Chemical Biology, Rutgers, The State University of New Jersey, 610 Taylor Road, Piscataway, New Jersey, 08854

[b]Waksman Institute of Technology, Rutgers, The State University of New Jersey, 190 Frelinghuysen Road, Piscataway, New Jersey, 08854

*Corresponding author (e-mail: dismukes@rutgers.edu).

†These authors contributed equally.

1. Powder X-Ray Diffraction

Powder X-Ray diffraction was conducted at room temperature on a Philips Xpert system, spinning at 100 rpm, in a Bragg-Brentano geometry, using Cu K-alpha 0.15418 nm x-rays, calibrated daily with a Si standard. The step size used for the diffraction patterns shown was 0.02°, and the scan speed 0.013°/s. The sample holder was 3 mm deep and ½" in diameter, completely filled with as-synthesized powder. Post-reaction PXRD was conducted on catalyst pellets containing 1 (w/w) % neutralized Nafion. The pellets, 2 cm in diameter and 2 mm thick, were extracted from the reactor, rinsed with ultrapure water, and mounted onto a sample holder. After the measurements, the patterns were translated to correct for the offset sample height.

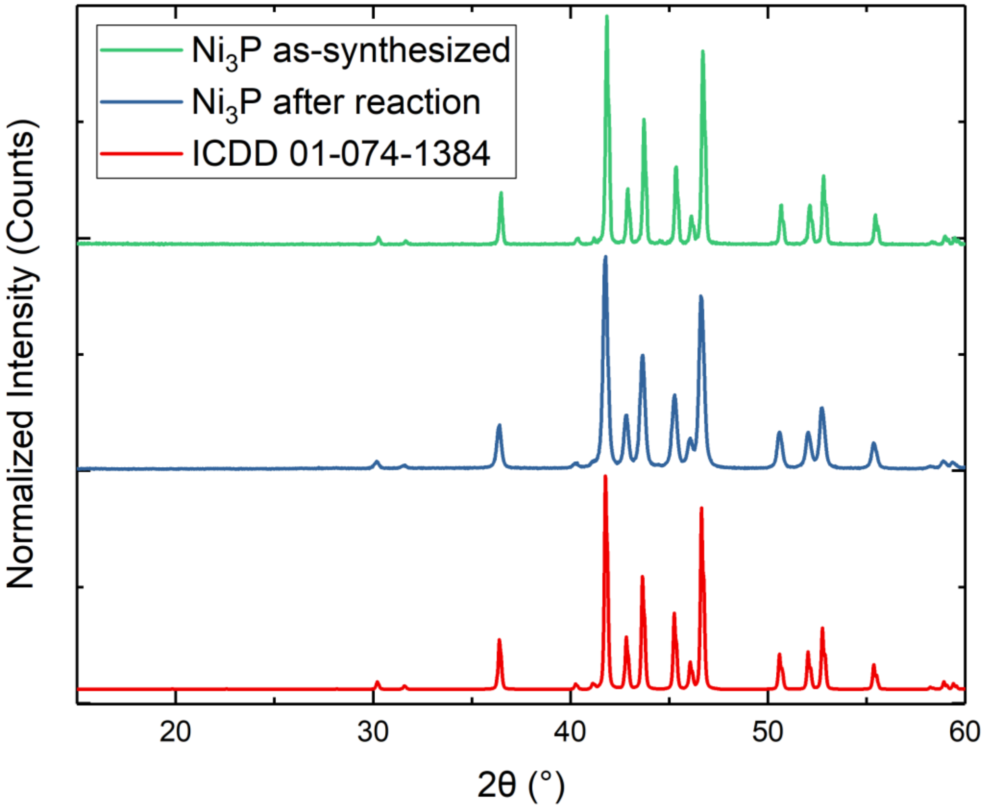

Figure S1 Powder X-ray diffraction of Ni_3P as-synthesized (top trace), after at least 3 hours of CO_2RR (middle trace) and simulated ICDD reference pattern (bottom trace). Pristine Ni_3P is crystalline and phase-pure. After reaction, no crystalline impurity is formed and crystallinity of the bulk structure of Ni_3P is preserved.

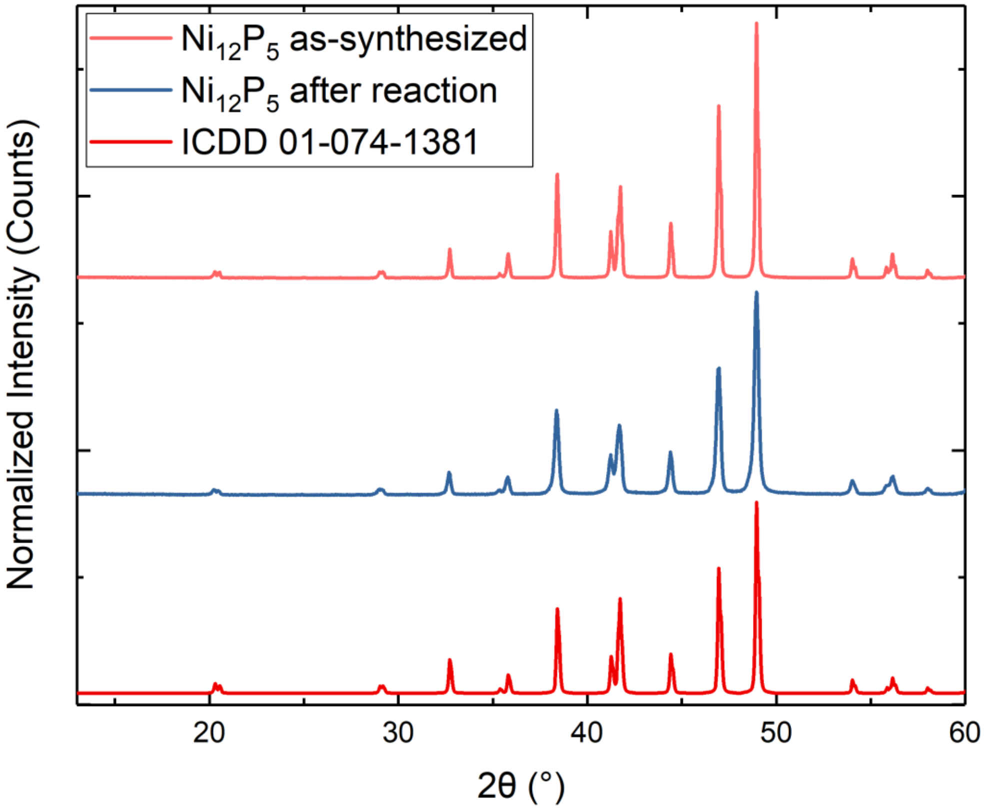

Figure S2: Powder X-ray diffraction of $Ni_{12}P_5$ as-synthesized (top trace), after at least 3 hours of CO_2RR (middle trace) and simulated ICDD reference pattern (bottom trace). Pristine $Ni_{12}P_5$ is crystalline and phase-pure. After reaction, no crystalline impurity is formed and crystallinity of the bulk structure of $Ni_{12}P_5$ is preserved.

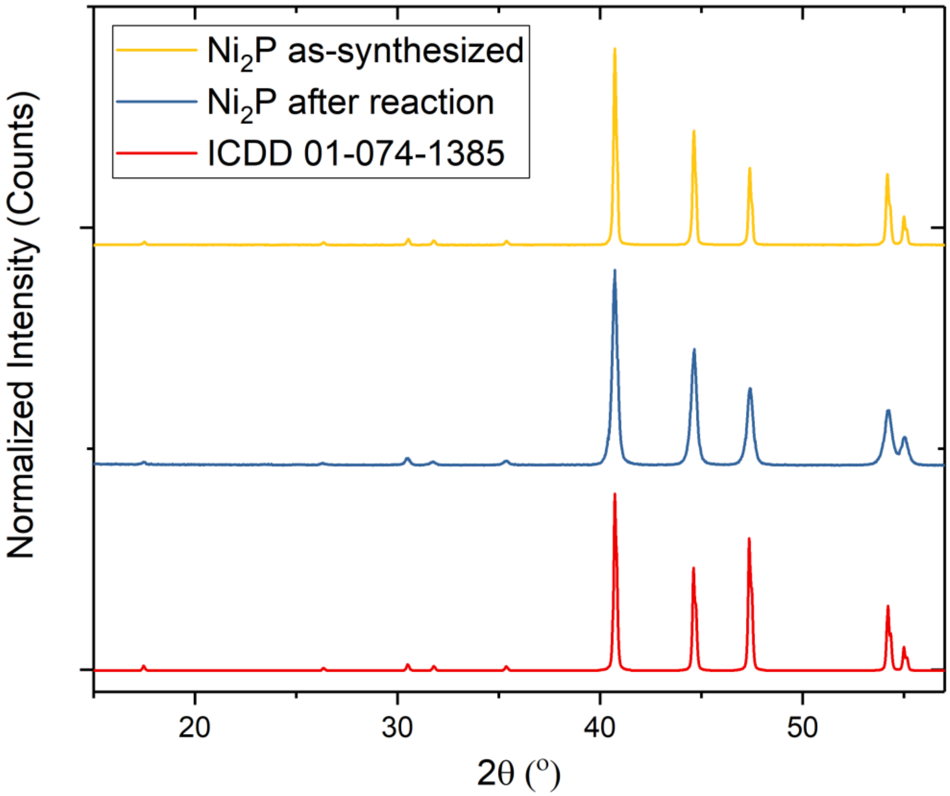

Figure S3: Powder X-ray diffraction of Ni_2P *as-synthesized (top trace), after at least 3 hours of* CO_2RR *(middle trace) and simulated ICDD reference pattern (bottom trace). Pristine* Ni_2P *is crystalline and phase-pure. After reaction, no crystalline impurity is formed and crystallinity of the bulk structure of* Ni_2P *is preserved.*

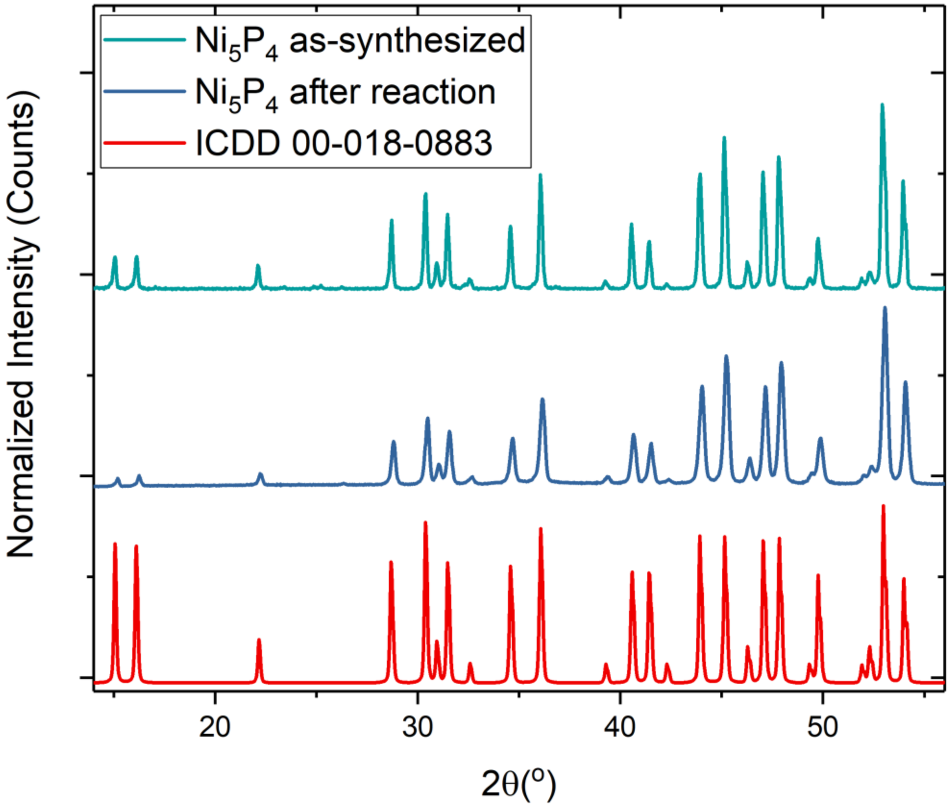

Figure S4 Powder X-ray diffraction of Ni_5P_4 as-synthesized (top trace), after at least 3 hours of CO_2RR (middle trace) and simulated ICDD reference pattern (bottom trace). Pristine Ni_5P_4 is crystalline and phase-pure. After reaction, no crystalline impurity is formed and crystallinity of the bulk structure of Ni_5P_4 is preserved.

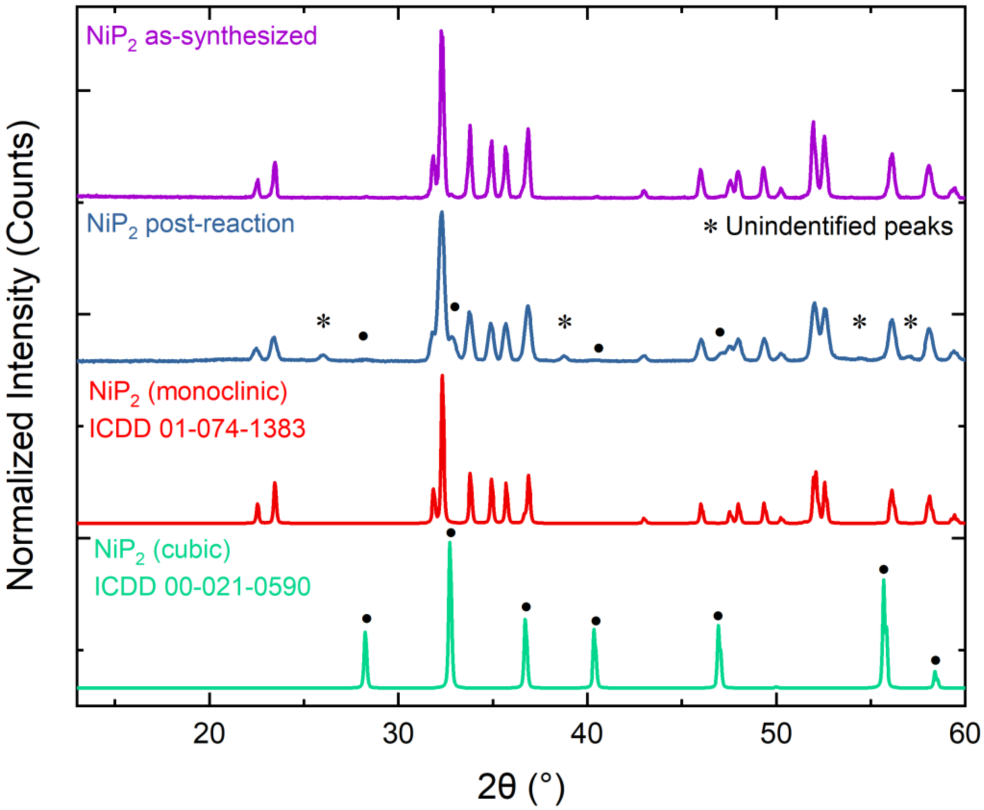

Figure S5: Powder X-ray diffraction of NiP_2 as-synthesized (purple trace), after 3 hours of CO_2RR (blue trace) and simulated ICDD reference pattern for the monoclinic (red trace) and cubic (mint green trace) polymorphs. Pristine NiP_2 is in the monoclinic crystalline polymorph. After reaction, while the crystalline structure is mostly preserved, 9% (calculated by the peak area ratio) of the monoclinic phase is converted to the cubic phase of NiP_2. Additionally, four new diffraction peaks appear. XPS indicates the presence of surface hydroxides and phosphates. The impurity peak at 38^o matches one of the 100% intensity peaks, the (101), in $Ni(OH)_2$ (ICDD 00-014-0117), but the other 100% intensity (001) peak at 19^o is missing. The lower intensity $Ni(OH)_2$ peaks coincide with the NiP_2 peaks and would not be resolved in the diffractogram. The three remaining impurity peaks match $Ni_3(PO_4)_2$ (ICDD 01-070-1796), including the major (111) line at 20^o and other peaks expected to be minor. Since the intensities expected of the phosphate and hydroxide pattern do not match perfectly the peaks that appear after reaction, the assignment of the impurity structure is uncertain by PXRD alone.

2. Scanning Electron Microscopy

The scanning electron micrographs shown below (Figure S6 and S7) were obtained using a Zeiss Sigma Field Emission SEM in-lens detector. The samples were supported on conductive carbon tape.

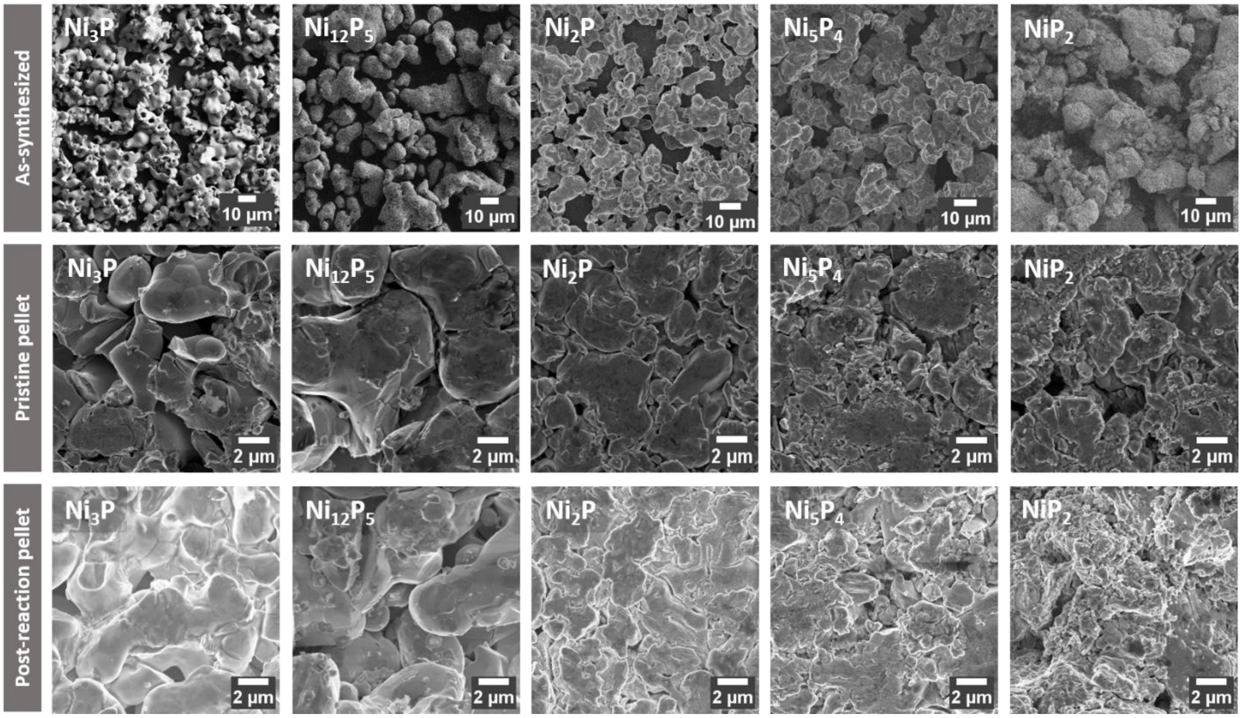

Figure S6: SEM images of as-synthesized nickel phosphide loose powders showing roughly spherical, polydisperse particles (top row). The second row of images shows the morphology of the particles after being pressed into pellets. After at least three CO_2RR turnovers per surface atom, the catalysts were imaged as pressed pellets (bottom row).

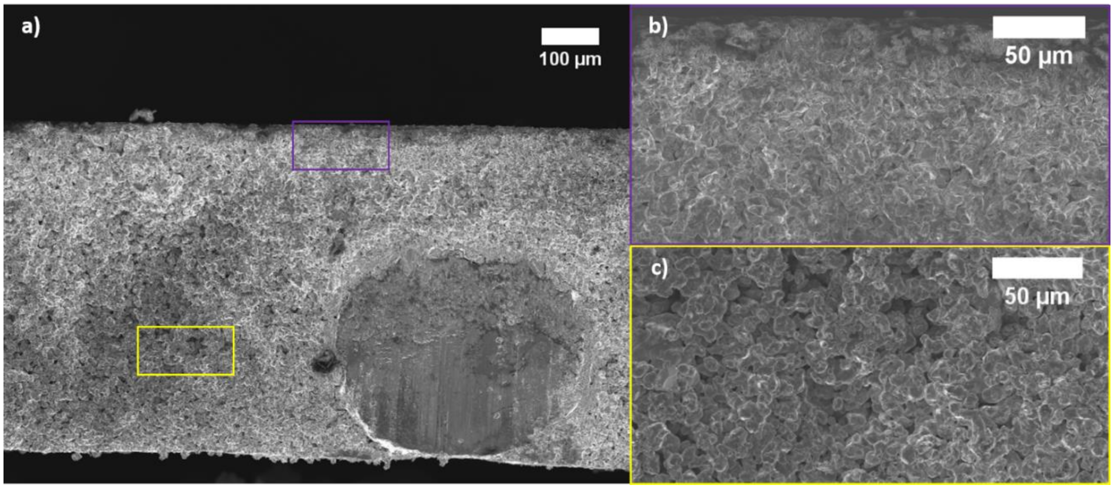

Figure S7: Cross-section SEM of a post-reaction Ni_2P pellet. From (a), the mean thickness of the pellet is 575 μm. The cylinder that appears on the lower right corner of image is from the aluminum mesh used for the pellet's mechanical support and faces away from the electrolyte. Inset (b) shows that, near the surface, the particles are packed more tightly than in the center of the pellet, (c).

3. Determination of uncompensated resistance

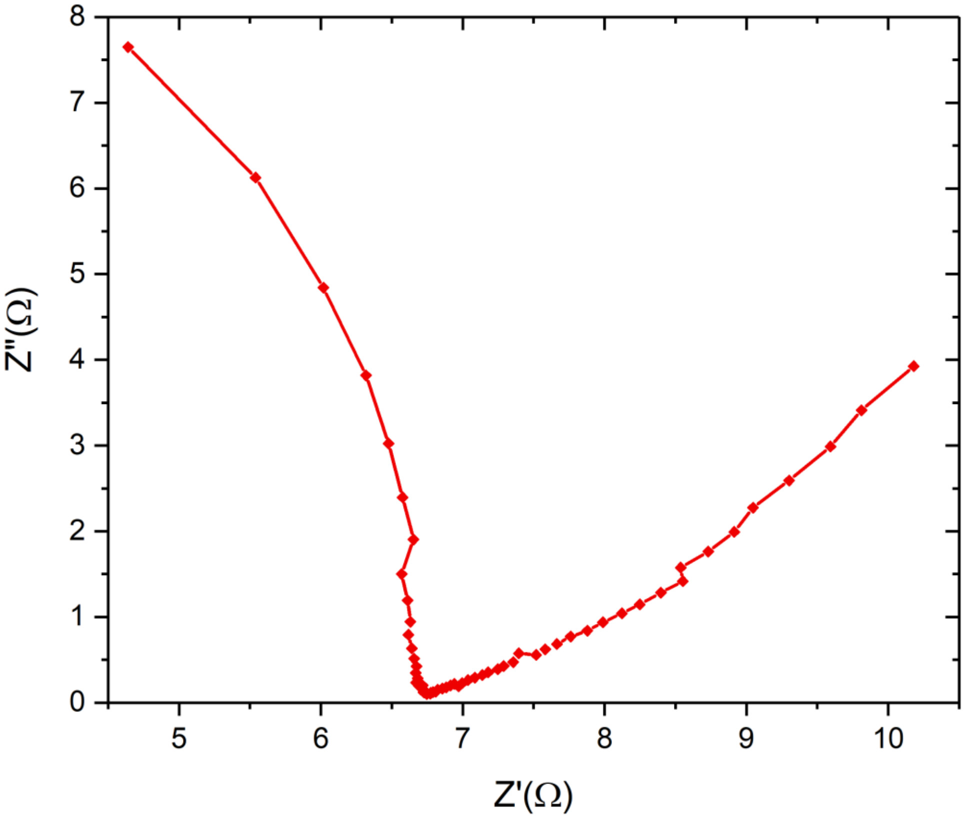

Figure S8: Potentiostatic electrochemical impedance spectroscopy of Ni_2P *at 0 V vs RHE in 0.5 M* $KHCO_3$ *gives a solution resistance of 6.75 Ω. This measurement was done before reaction and is representative of the behavior observed for all of the tested nickel phosphides.*

4. Electrochemical surface area measurements

Electrochemical capacitance was utilized to determine the surface area of each of the nickel phosphides. To measure capacitance, the potential was cycled between 0.11 and -0.04 V vs RHE at different scan rates in CO_2-saturated 0.5M $KHCO_3$. The cyclic voltammograms for Ni_2P can be seen in Figure S9. The capacitive current was measured at 0.04 V, where the faradaic current is minimal, and plotted versus scan rate. The slope of the linear fit is the capacitance of the sample. The electrochemical surface area (ECSA) was calculated using the ratio of the capacitance measured and the specific capacitance for metal phosphides (40 µF/cm², as reported by Kibsgaard *et al*[1]). A roughness factor was then obtained by dividing the ECSA by the geometric area of the sample.

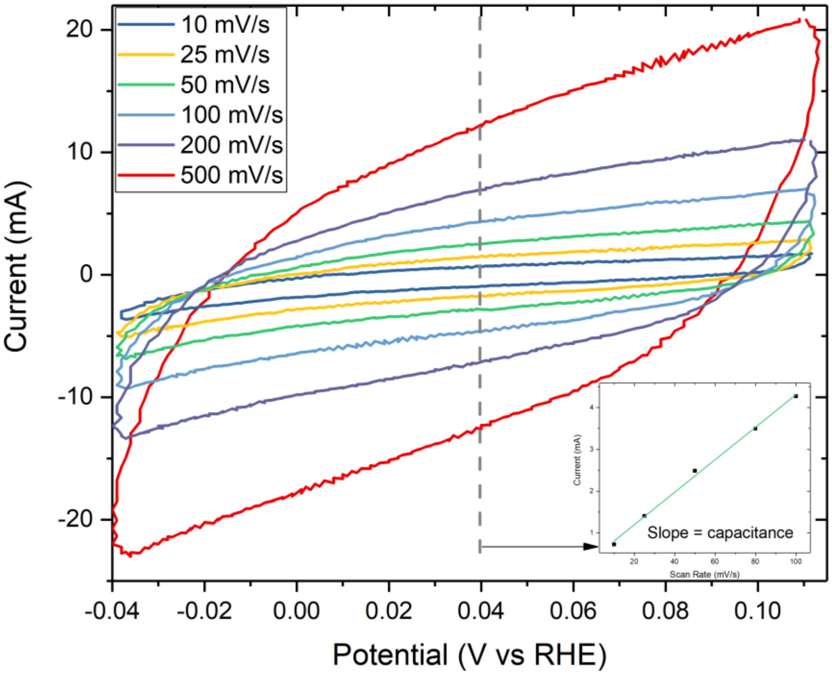

Figure S9: Electrochemical capacitance measurement to determine the surface area of Ni_2P. The capacitive current is determined from cyclic voltammograms in a region with minimal Faradaic current (in this case 0.04 V). In the inset, the capacitive current is plotted as a function of scan rate.

Table S1: Roughness factors calculated from the electrochemical surface area

Catalyst	Roughness Factor
Ni_3P	276
$Ni_{12}P_5$	158
Ni_2P	312
Ni_5P_4	214
NiP_2	349

5. Linear Sweep Voltammetry

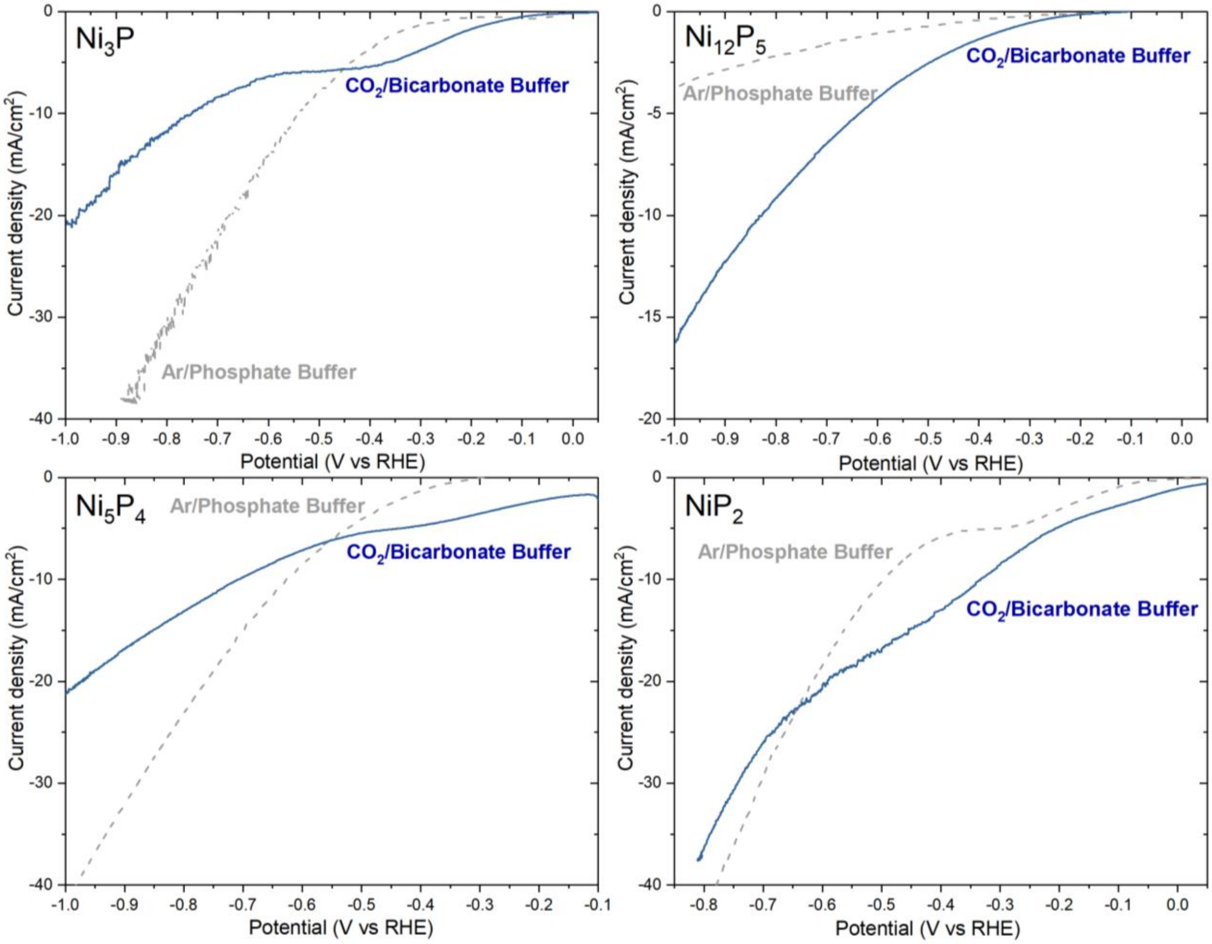

Figure S10: Linear sweep voltammetry of Ni_3P, $Ni_{12}P_5$, Ni_5P_4, and NiP_2 in CO_2 saturated 0.5 M $KHCO_3$ (blue) and argon-purged 0.5 M phosphate buffer solution. The scan rate used was 0.5 mV/s and the solution resistance was compensated through positive feedback.

6. Chronoamperometry

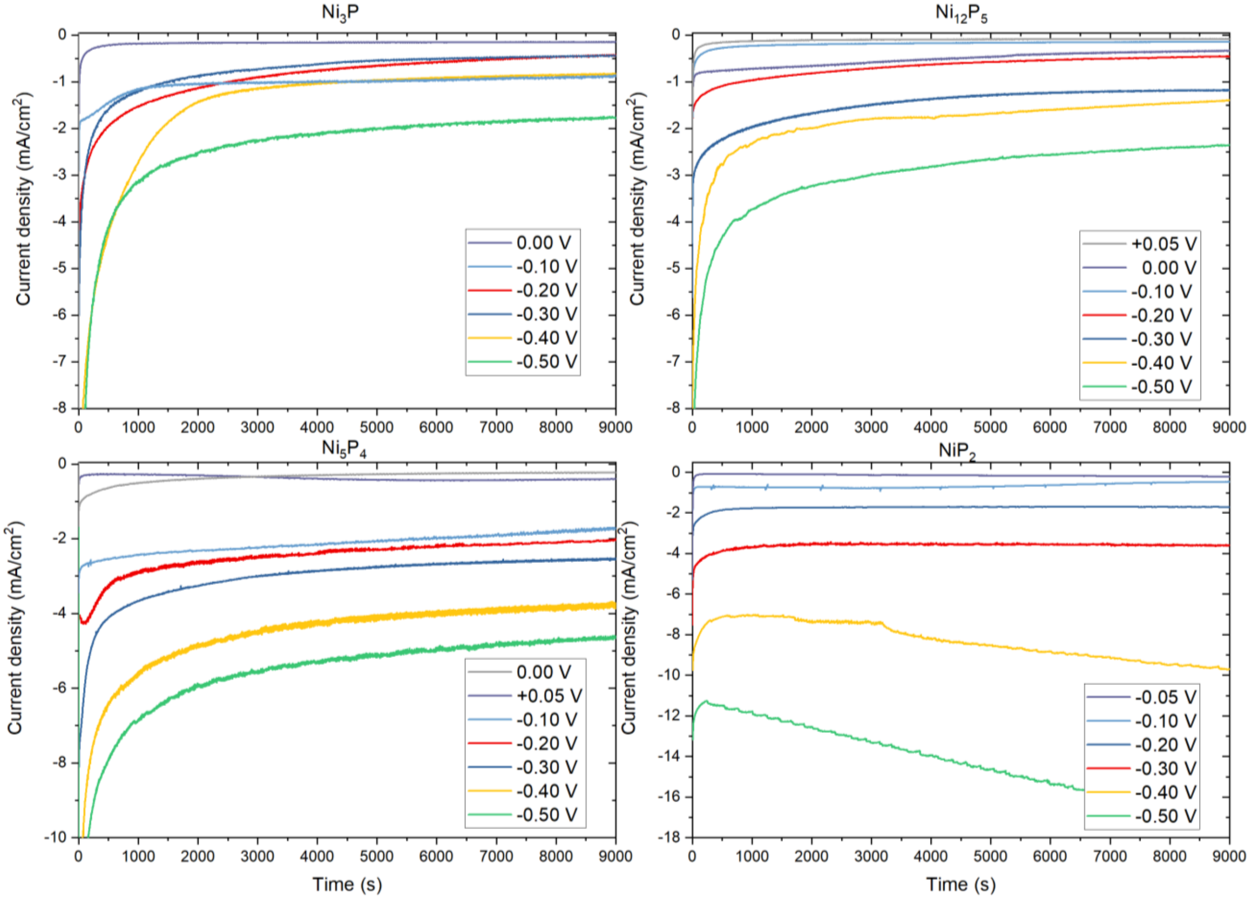

Figure S11: Representative IR-compensated chronoamperometry measurements in CO_2-purged (5 sccm) 0.5 M $KHCO_3$.

7. Gas Chromatrography

Detection and quantification of possible headspace products (Hydrogen, carbon monoxide, carbon dioxide, methane, ethane, and ethylene) was performed by an auto-sampling online HP 5890 Series II GC, with a 500 µL sample loop. The GC was fitted with a 6’ packed HayeSep D, and a 6’ packed MoleSieve 13X column, with thermal conductivity and flame ionization detectors connected in series. Argon was used as the carrier gas. The temperature was held at 50^{o}C for 5 minutes for the desorption of permanent gases, then increased at a rate of 20 ^{o}C/min for 10 min for desorption of C_2 hydrocarbons, CO and CO_2, finishing with a 2 minute hold at 250 ^{o}C to ensure full elution of possible water vapor. Quantification limits were 2 ppm for C_2H_6 and C_2H_4, 5 ppm for CH_4, 50 ppm for H_2, 200 ppm for O_2 and N_2, and 600 ppm for CO_2 and CO.

Samples were taken before reaction to check for air presence and then every 30 minutes thereafter. Calibration curves were constructed from certified gas standards (Gasco) by CO_2 dilution using MKS P4B mass flow controllers (MFCs). The hydrogen calibration was done with *in situ* generated gas through electrolysis of water on platinum, under argon purge, and diluted post-reaction with CO_2.

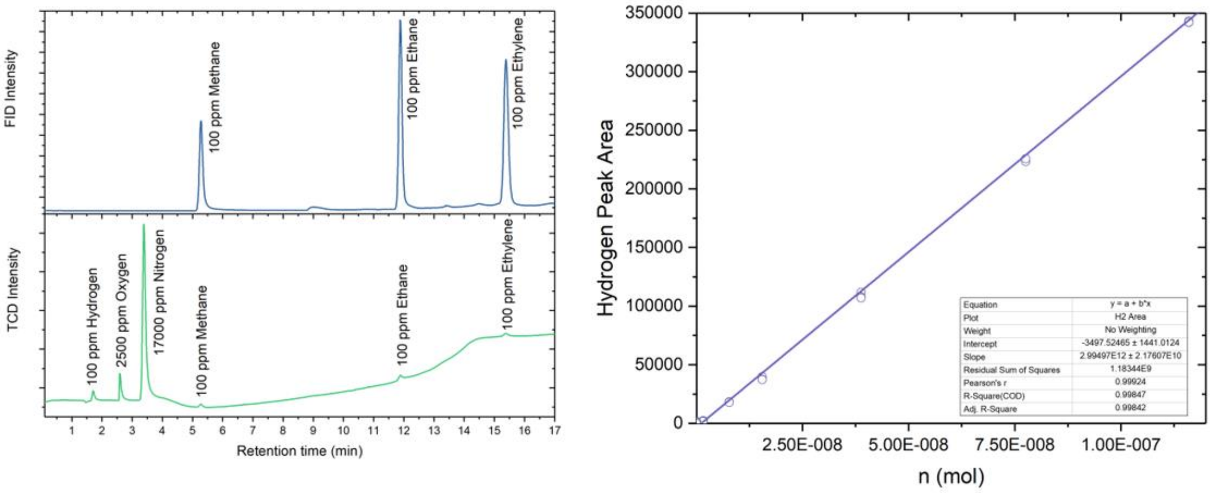

Equation	y = a + b*x
Plot	H2 Area
Weight	No Weighting
Intercept	-3497.52465 ± 1441.0124
Slope	2.99497E12 ± 2.17607E10
Residual Sum of Squares	1.18344E9
Pearson's r	0.99924
R-Square(COD)	0.99847
Adj. R-Square	0.99842

Figure S12: (A) Typical chromatograph resulting from a mixed calibration standard (Gasco 105L-508). The quantification limits are 100 ppm (B) Calibration curve for hydrogen, the only product detected in the gas phase.

8. Liquid Product Analysis by ^{1}H NMR/COSY

^{1}H NMR spectra was recorded using a Bruker Avance III 700 MHz NMR spectrometer equipped with a cryoprobe. 400 μL samples from the CO_2 reduction electrolyte were taken after the reaction from the working electrode compartment. The samples were combined with 100 μL of D_2O. Correlation spectra (COSY) were also recorded on the samples to assist in the ^{1}H.

While the assignment of the formic acid peak was straightforward, the same was not true for the other two products. Based on the molecular structure, one would expect to see doublet peaks for 2,3-furandiol with coupling constants of J = 1.75 Hz. However, owing to the linewidths in aqueous solvent, they appear as singlets. For methylglyoxal, the complications arise from its high reactivity: in water, methylglyoxal forms mono-hydrates, di-hydrates, dimers and trimers. The ^{1}H NMR of methylglyoxal in aqueous solution and its derivatives has been reported by Nemet *et al*[2]; the corresponding predicted shifts are reported in the table below.

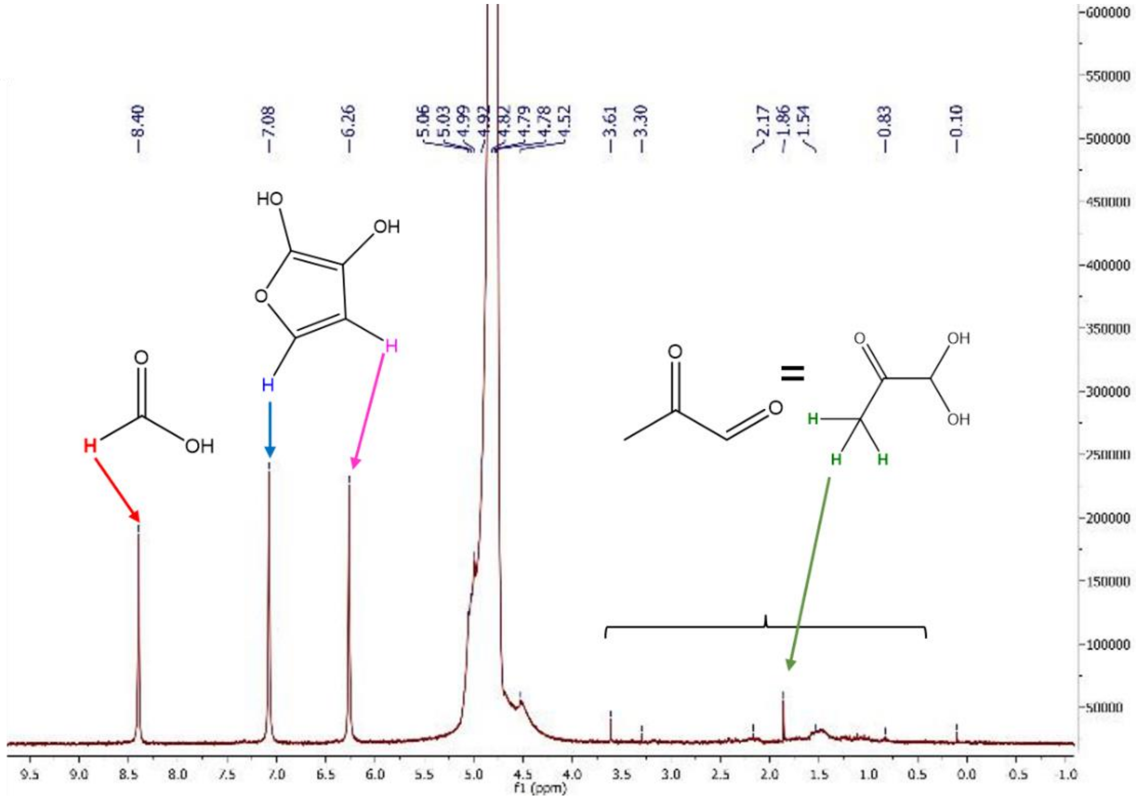

Figure S13: ^{1}H NMR of an electrolyte sample from the electroreduction of CO_2 on Ni_5P_4.

Table S2: Predicted ^1H NMR shifts for 2,3-furandiol and methylglyoxal species.

Compound	**Predicted delta (ppm)**[3,4]	**Compound**	**Predicted delta (ppm)**[3,4]
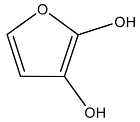	6.145 (d), J = 0.0025 ppm 7.030 (d), J = 0.0025 ppm	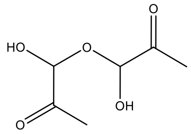	2.095 (s) 5.726 (s)
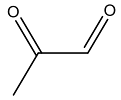	2.067 (s) 9.560 (s)	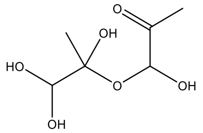	1.231 (s) 2.098 (s) 4.890 (s) 5.825 (s)
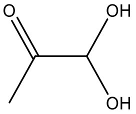	2.083 (s) 5.441 (s)	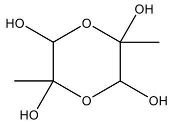	1.301 (s) 4.415 (s)
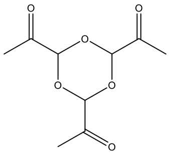	2.100 (s) 5.378 (s)	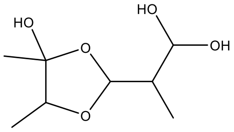	1.286 (s) 1.391 (s) 3.476 (d) 3.996 (t) 4.464 (s)
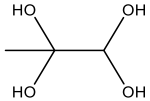	1.112 (s) 4.871 (s)		

9. Liquid Chromatography - Mass Spectrometry

Reaction products were analyzed by injecting 10 uL of electrolyte into an Agilent 1200 series HPLC coupled to an Agilent 6490 QQQ mass spectrometer equipped with an ion-spray source. Products were separated utilizing an Aminex HPX-87H column, using isocratic elution with 5 mM sulfuric acid in LCMS-grade water at a flow rate of 0.2 mL min-1. Mass spectral operating parameters were set as described by Bennette et al.[5] The MS scan was performed in negative ion mode over a range of mass-to-charge ratios between 30 and 195 m/z. The acquired data was analyzed using Agilent Mass Hunter software v. 1.04.

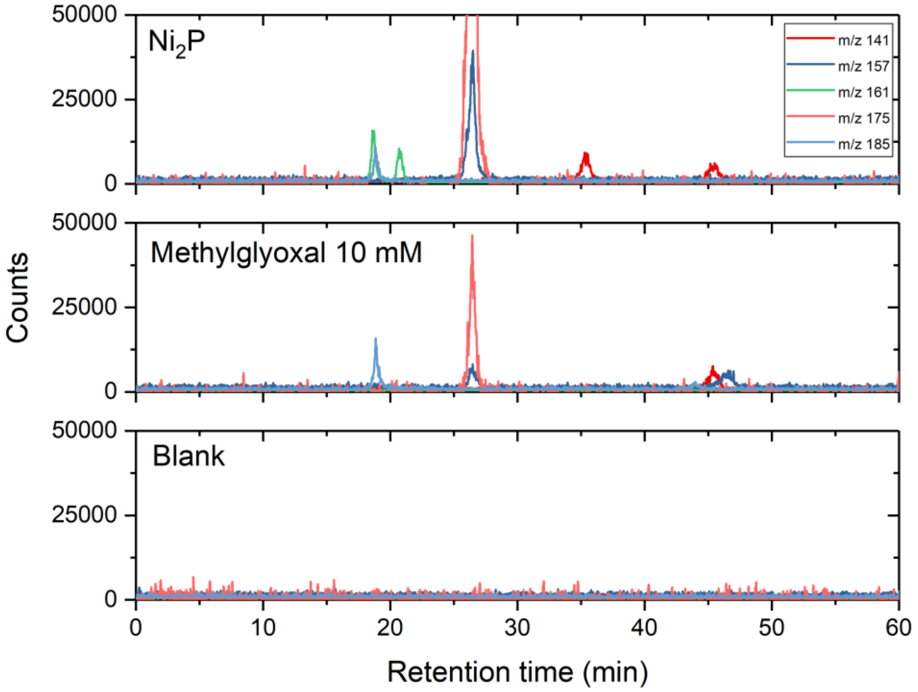

Figure S14: LC-MS of a -0.1 V vs RHE Ni2P sample. The unretained peak is at 19 min, followed by 2,3-furandiol and methylglyoxal. As methylglyoxal undergoes self-condensation in solution, several peaks are observed for it. Assignment of the LC-MS mass-to-charge ratios is shown in the table below.

Table S3: Interpretation of LCMS based on reference [6]

Molecule	**Molecular Formula**	**MW**	**m/z**	**Retention time (min)**	**Comment**
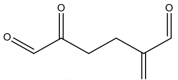	$C_6H_6O_4$	142.1	141	45.5	Methylglyoxal dimer (condensation product of methylglyoxal)
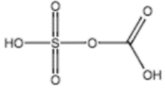	CH_2O_5S			35.5	Sulfuric acid + formic acid
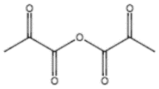	$C_6H_6O_5$	158.1	157	26.7	Condensation product of methylglyoxal
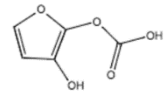 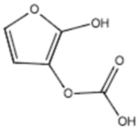	$C_5H_4O_5$	144.1	161	18.2, 20.8	2,3-furandiol and carbonic acid ester + H_2O
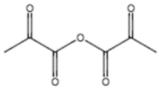	$C_6H_6O_5$	158.1	175	26.5	Condensation product of methylglyoxal + water
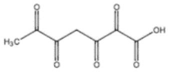	$C_7H_6O_6$	186.1	185	18.5	2 x methylglyoxal + formic acid (condensation product of methylglyoxal)

10. High Performance Liquid Chromatography

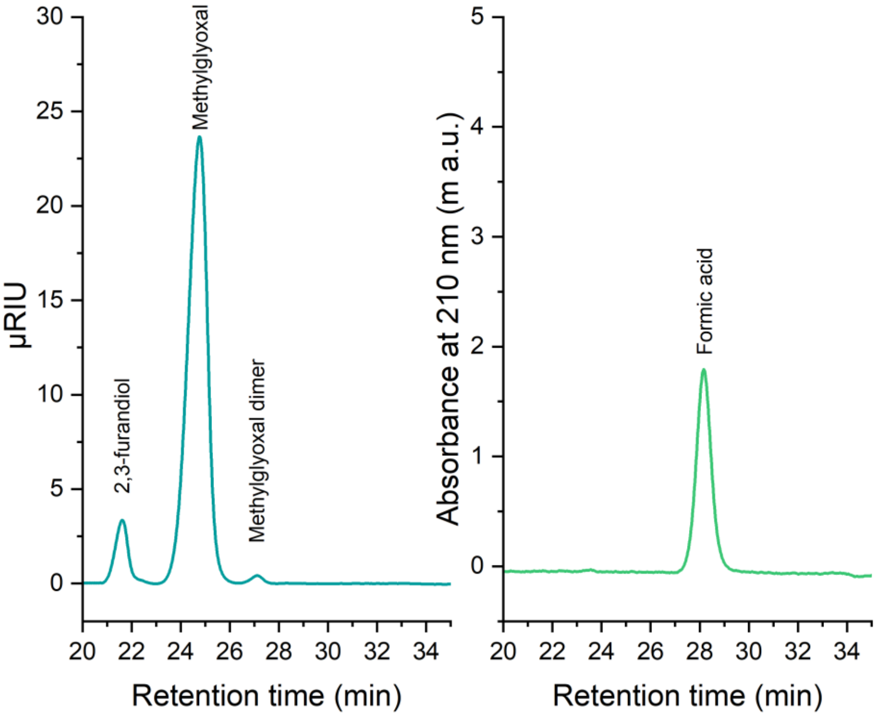

Figure S15: Example of chromatographs for a CO_2RR sample on Ni_2P at -0.1 V vs RHE obtained with the refractive index detector (left) and the UV absorbance detector (right), arranged in series.

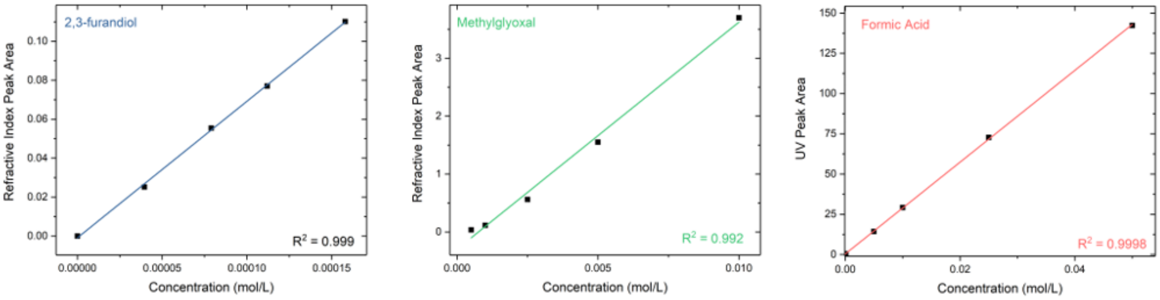

Figure S16: Calibration curves (from left to right) for 2,3-furandiol, methylglyoxal and formic acid. The mean error associated with the HPLC quantification was determined to be <2%.

11. Method for 2,3-furandiol quantification

Due to the difficulty in purchasing analytical standards of 2,3-furandiol, we quantitively determined the concentration of the analyte in one CO_2RR electrolyte sample via ^1H-NMR using a Bruker Avance III 700 MHz. This NMR spectrometer was equipped with a cryoprobe. The sample was then considered a 2,3-furandiol standard and diluted to build a calibration curve for the HPLC-RID, used as the routine quantification tool. The retention time of 2,3-furandiol was confirmed through LCMS. For the NMR calibration, five solutions of 510 μL were prepared to determine a curve for the 2,3-furandiol product. The CO_2RR electrolyte containing 2,3-furandiol was diluted to 400 μL in 0.5 M $KHCO_3$ in electrolyte:bicarbonate ratios of 1:0, 1:1, 1:2, 1:3, and 0:1 (blank), to which 100 μL of D_2O and 10 μL of acetonitrile were added. The acetonitrile, which has a single peak at 2.00 ppm, was utilized as an internal standard to quantify 2,3-furandiol in the liquid products through the baseline-subtracted peak area ratio. The acetonitrile did not interfere with the 2,3-furandiol peaks, which occur at 6.26 and 7.03 ppm respectively. The concentration of 2,3-furandiol in the electrolyte was calculated from the equation of the linear fit, shown below to be 140 μmol/L.

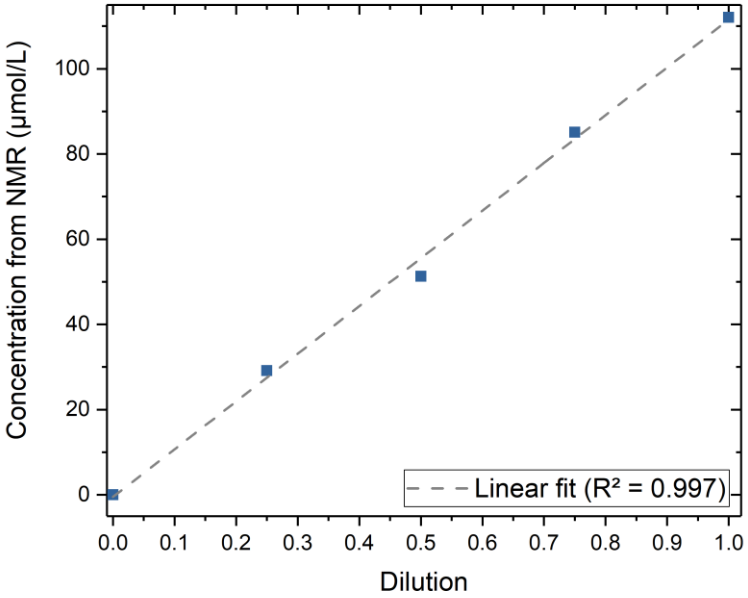

Figure S17: Concentration of 2,3-furandiol in a CO_2RR electrolyte sample as measured by NMR as a function of sample dilution.

12. Faradaic Efficiency

The Faradaic Efficiency for the liquid CO_2 reduction products was calculated using the equation:

$$FE_{CO2RR} = \frac{Concentration \cdot V_{electrolyte} \cdot \#electrons \cdot F}{Charge}$$

where the concentration was measured by HPLC; the volume of electrolyte measured after each experiment (around 6 mL); the number of electrons is 2 for formate, 12 for methylglyoxal and 14 for furandiol; F is Faraday's constant and the charge was integrated over the full time of the experiment. Each value in the table below reflects the average of at least three measurements.

To determine the hydrogen Faradaic Efficiency, on-line measurements were conducted, and the following equation was used:

$$FE_{H2} = \frac{mols\ of\ H2 \cdot \#electrons \cdot F}{current \cdot time}$$

Where the number of mols of hydrogen was determined by GC, the number of electrons is 2, the current is recorded at the instant of automated sampling, and the time is what is required to fill up the GC sample loop (3 s at 5 sccm). Each value in the table below reflects the average of at least 5 measurements.

Table S4: Faradaic efficiency for all catalysts at the potentials tested ± standard deviation between at least three chronoamperometry experiments.

	Potential (V vs RHE)	Formate Faradaic Efficiency (%)	2,3-furandiol Faradaic Efficiency (%)	Methylglyoxal Faradaic Efficiency (%)	CO_2RR FE (%)	Hydrogen Faradaic Efficiency (%)	Total FE (%)
Ni_3P	0.00	4.06 ± 0.06	2.06 ± 0.03	2.34 ± 0.04	8.46	89.7 ± 34.2	98.2
	-0.10	4.37 ± 0.07	3.35 ± 0.05	1.83 ± 0.03	9.55	91.1 ± 10.6	100.7
	-0.20	3.60 ± 0.06	2.92 ± 0.05	1.81 ± 0.03	8.33	85.4 ± 16.6	93.7
	-0.30	1.69 ± 0.03	1.88 ± 0.03	2.51 ± 0.04	6.08	94.0 ± 15.6	100.1
	-0.40	2.75 ± 0.04	2.88 ± 0.05	4.05 ± 0.06	9.69	90.5 ± 6.90	100.2
	-0.50	0.90 ± 0.01	1.24 ± 0.02	1.87 ± 0.03	4.01	96.3 ± 7.41	100.3
$Ni_{12}P_5$	0.05	0.47 ± 0.01	22.1 ± 0.35	15.0 ± 0.24	37.5	62.3 ± 2.87	99.8
	0.00	0.44 ± 0.01	32.8 ± 0.52	32.4 ± 0.52	65.6	34.6 ± 6.55	100.2
	-0.10	1.41 ± 0.02	2.54 ± 0.04	7.03 ± 0.11	11.0	88.2 ± 4.31	99.2
	-0.20	2.43 ± 0.04	6.41 ± 0.10	8.61 ± 0.14	17.5	82.5 ± 7.07	99.9
	-0.30	0.07 ± 0.00	0.11 ± 0.00	1.38 ± 0.02	1.56	94.5 ± 13.1	96.1
	-0.40	0.47 ± 0.01	0.65 ± 0.01	1.31 ± 0.02	2.43	96.3 ± 7.21	98.7
	-0.50	0.29 ± 0.00	0.38 ± 0.01	0.91 ± 0.01	1.58	99.6 ± 5.62	101.2
Ni_2P	0.05	1.51 ± 0.02	4.65 ± 0.07	42.3 ± 0.68	48.4	46.3 ± 13.2	94.7
	0.00	1.61 ± 0.03	71.6 ± 1.15	27.1 ± 0.43	100.3	0.0 ± 2.78	100.3
	-0.10	0.61 ± 0.01	9.94 ± 0.16	3.17 ± 0.05	13.7	86.6 ± 3.76	100.4
	-0.20	0.00 ± 0.00	10.8 ± 0.17	4.55 ± 0.07	15.4	84.7 ± 5.19	100.0
	-0.30	0.52 ± 0.01	2.53 ± 0.04	2.05 ± 0.03	5.1	92.2 ± 15.6	97.3
	-0.40	2.48 ± 0.04	7.17 ± 0.11	2.28 ± 0.04	12.0	88.4 ± 14.8	100.3

	Potential (V vs RHE)	Formate Faradaic Efficiency (%)	2,3-furandiol Faradaic Efficiency (%)	Methylglyoxal Faradaic Efficiency (%)	CO_2RR FE (%)	Hydrogen Faradaic Efficiency (%)	Total FE (%)
	-0.50	1.35 ± 0.02	1.19 ± 0.02	0.78 ± 0.01	3.32	92.0 ± 15.7	95.3
Ni_5P_4	0.05	1.11 ± 0.01	34.3 ± 0.40	45.4 ± 0.65	80.8	16.2 ± 13.4	97.0
	0.00	2.56 ± 0.04	9.00 ± 0.14	9.12 ± 0.15	20.7	78.6 ± 15.6	99.3
	-0.10	2.44 ± 0.04	9.97 ± 0.16	3.77 ± 0.06	16.2	82.2 ± 14.9	98.4
	-0.20	0.37 ± 0.01	3.42 ± 0.05	3.91 ± 0.06	7.70	87.8 ± 15.1	95.5
	-0.30	0.71 ± 0.01	3.17 ± 0.05	4.04 ± 0.06	7.92	87.5 ± 13.4	95.4
	-0.40	0.65 ± 0.01	1.93 ± 0.03	0.91 ± 0.01	1.88	97.3 ± 13.7	99.2
	-0.50	0.62 ± 0.01	1.30 ± 0.02	0.61 ± 0.01	2.52	93.6 ± 3.65	96.1
NiP_2	-0.05	0.22 ± 0.00	39.3 ± 0.63	61.1 ± 0.98	100.6	0.1 ± 0.10	100.7
	-0.10	0.10 ± 0.00	16.2 ± 0.26	84.4 ± 1.35	100.7	3.9 ± 3.64	104.6
	-0.20	0.02 ± 0.00	0.90 ± 0.01	1.76 ± 0.03	2.67	94.1 ± 3.81	96.8
	-0.30	0.03 ± 0.00	1.31 ± 0.02	7.65 ± 0.12	10.6	87.1 ± 3.21	97.8
	-0.40	0.01 ± 0.00	0.40 ± 0.01	0.56 ± 0.01	0.96	92.6 ± 0.49	93.5
	-0.50	0.01 ± 0.00	0.19 ± 0.00	0.17 ± 0.00	0.36	98.5 ± 3.75	98.9

13. Partial Current Density

Table S5: Partial current densities for all catalysts. Currents were recorded after 3 hours of chronoamperometry and multiplied by the faradaic efficiency for each product.

Catalyst	Potential (V vs RHE)	j_{Total} (mA/cm^2)	$j_{Formate}$ (μA/cm^2)	$j_{Methylglyoxal}$ (μA/cm^2)	$j_{Furandiol}$ (μA/cm^2)	j_{CO2RR} (μA/cm^2)	j_{HER} (μA/cm^2)
Ni_3P	0	-0.15	-6.01	-3.46	-3.05	-12.52	-132.76
	-0.1	-0.85	-37.32	-15.63	-28.61	-81.56	-777.99
	-0.2	-0.42	-15.12	-7.60	-12.26	-34.99	-358.68
	-0.3	-0.42	-7.10	-10.54	-7.90	-25.54	-394.80
	-0.4	-0.86	-23.54	-34.67	-24.65	-82.86	-774.68
	-0.5	-1.75	-15.75	-32.73	-21.70	-70.18	-1,685.25
$Ni_{12}P_5$	0.05	-0.08	-0.38	-12.15	-17.90	-30.43	-50.46
	0	-0.33	-1.46	-107.24	-108.57	-217.27	-114.53
	-0.1	-0.08	-1.18	-5.91	-2.13	-9.22	-74.09
	-0.2	-0.45	-11.03	-39.09	-29.10	-79.22	-374.55
	-0.3	-1.80	-1.26	-24.84	-1.98	-28.08	-1,701.00
	-0.4	-1.41	-6.63	-18.47	-9.17	-34.26	-1,357.83
	-0.5	-2.37	-6.87	-21.57	-9.01	-37.45	-2,360.52
Ni_2P	0.05	-0.04	-0.59	-16.57	-1.82	-18.98	-18.14
	0	-0.03	-0.50	-8.42	-22.25	-31.17	0.00
	-0.1	-0.14	-0.86	-4.48	-14.06	-19.40	-122.45
	-0.2	-0.04	0.00	-1.78	-4.23	-6.01	-33.18
	-0.3	-0.56	-2.92	-11.52	-14.22	-28.67	-518.26
	-0.4	-2.77	-68.63	-63.10	-198.43	-330.16	-2,446.48
	-0.5	-3.50	-47.29	-27.32	-41.69	-116.31	-3,222.93
Ni_5P_4	0.05	-0.42	-4.63	-189.32	-143.03	-336.98	-67.55
	0	-0.23	-5.94	-21.16	-20.88	-47.98	-182.35
	-0.1	-1.71	-41.72	-64.47	-170.49	-276.68	-1,405.62
	-0.2	-2.06	-7.62	-80.55	-70.45	-158.62	-1,808.68
	-0.3	-2.57	-18.25	-103.83	-81.47	-203.54	-2,248.75
	-0.4	-3.82	-24.84	-34.78	-73.76	-133.38	-3,718.47
	-0.5	-4.59	-28.46	-28.00	-59.67	-116.13	-4,296.24
NiP_2	-0.05	-0.21	-0.46	-127.70	-82.14	-210.30	-0.21
	-0.1	-0.44	-0.44	-373.89	-71.77	-446.10	-17.28
	-0.2	-1.71	-0.34	-30.10	-15.39	-45.83	-1,609.11
	-0.3	-3.60	-1.08	-275.30	-47.14	-323.53	-3,134.49
	-0.4	-9.68	-0.97	-54.22	-38.73	-93.91	-8,965.10
	-0.5	-15.64	-1.56	-26.59	-29.72	-57.87	-15,405.4

14. Control Experiments

To determine if any organic products detected during the experiments could have originated from the degradation of the membrane, the body of the cell (Nylon 66), or the ionomer used in the electrode preparation, we performed a selection of control experiments. First, the cell was assembled, filled out with 0.25 M pyrophosphate buffer, and purged with argon. A typical Ni_2P pellet containing 1% Nafion was used as the working electrode. A sample of the electrolyte was taken after 1h of purge, then 24h, with no potential applied. No carbon-containing products were detected by HPLC nor by NMR.

Next, using the same experimental configuration, electrolysis was performed at -0.20 V vs RHE for 6h to determine if any products could have resulted from reductive degradation of the cell, membrane, or ionomer. Again, no organic compounds were detected by NMR, nor by HPLC.

Finally, we performed isotope labeling experiments, described below in Section 14, which show that the C_1, C_3, and C_4 products originate from dissolved inorganic carbon.

15. ^{13}C Isotopic Labeling

To confirm that the origin of the products described was indeed dissolved inorganic carbon (CO_2 or HCO_3^-) and not a contamination from other sources, such as the membrane or the electrolyzer body, we conducted an electrolysis experiment on Ni_2P at 0.00 V vs RHE using ^{13}C labeled bicarbonate. 1.000 g of $NaH^{13}CO_3$ (98 atom % ^{13}C, 99% chemically pure, Sigma Aldrich) was diluted with 25 mL of argon-purged ultra-pure water to form a 0.475 M labeled bicarbonate solution. The cell was immediately filled with 7 mL of solution in each compartment, purged with argon for 20 min at 5 sccm, and sealed with an airlock. We then proceeded to electrolyze the solution for 38h. The total amount of products formed was quantified via HPLC: 0.22 mM of formate, 2.51 mM of 2,3-furandiol and 1.73 mM of methylglyoxal.

Surface-Assisted Laser Desorption/Ionization time-of-flight mass spectrometry (SALDI TOF-TOF-MS) was performed to quantify the ratio of ^{13}C to ^{12}C in the products formed. The instrument used was a Bruker Daltonics Autoflex III Smartbeam mass spectrometrer equipped with a 355 nm Nd:YAG laser. Samples were exposed to 500 laser shots fired at a frequency of 100 Hz at typically 25-45% of full laser power in a random walk pattern to produce integrated spectra. The instrument was operated in reflectron mode with a mass range of 50-1200 Da. The samples were prepared by pipetting 1 µL of electrolyte onto a specially prepared gold-sputtered stainless-steel plate. The background was verified to be negligible and the signal-to-noise ratio was at least 10 for all peaks shown. All data were analyzed with Bruker Daltonics flexAnalysis software and mMass. The mass spectrometer was calibrated internally using the gold.

As shown in Figure S18 and Table S5, both methylglyoxal and furandiol are labeled with ^{13}C, indicating that the source of carbon for both the products is dissolved inorganic carbon. The calculated ratio of $^{12}C/^{13}C$ on furandiol is 1.77%, consistent with the nominal 2 atom % ^{12}C on the sodium bicarbonate used as the carbon source. However, melthylglyoxal is particularly very reactive in water, and forms oligomers and hydrates as indicated in the table below, complicating the quantification of ^{13}C incorporation in that product.

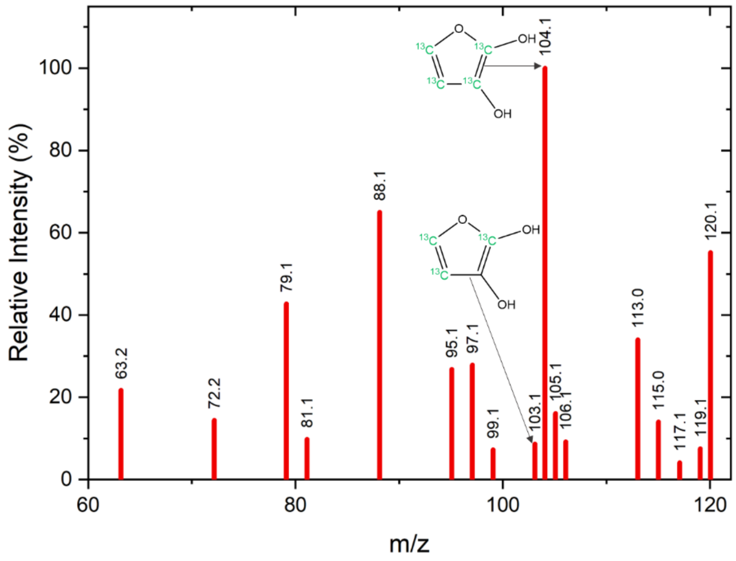

Figure S18: SALDI-TOF of sample from electrolysis of $NaH^{13}CO_3$ on Ni_2P at 0.00 V vs RHE

Table S5: Assignment of mass peaks obtained by SALDI-TOF to molecular ions and adducts

Measured m/z	Calculated m/z	Intensity	Relative Intensity (%)	Annotation	Formula
63.17	63.02	526.04	21.67	^{13}C bicarbonate [M+H]	$H^{13}CO_3$
72.15	72.03	349.63	14.41	^{12}C methylglyoxal	$^{12}C_3H_4O_2$
79.12	78.52	1036.11	42.69	$^{13}C_3$ methylglyoxal [M+2H$_2$O+2Na]	$^{13}C_3H_4O_2$
88.12	88.04	1577.20	64.98	^{13}C methanediol (HCOOH +H$_2$O)	$^{13}C\ H_4O_2$
95.08	95.02	650.32	26.79	^{12}C methylglyoxal [M+Na]	$^{12}C_3H_4O_2$
97.07	97.02	676.43	27.87	$^{13}C_2{}^{12}C$ methylglyoxal [M+Na]	$^{13}C_2{}^{12}CH_4O_2$
103.10	103.03	210.45	8.67	$^{13}C_3{}^{12}C$ furandiol	$^{13}C_3{}^{12}CH_4O_3$
104.08	104.03	2427.04	100.00	$^{13}C_4$ furandiol	$^{13}C_4H_4O_3$
105.09	105.04	390.87	16.10	$^{13}C_4$ furandiol [M+H]	$^{13}C_4H_4O_3$
106.07	105.99	223.65	9.22	$^{13}C_2$ acetic acid [M+2Na-H]	$^{13}C_2H_4O_2$
113.02	113.03	824.54	33.97	$^{12}C_3$ methylglyoxal[M+H$_2$O+Na]	$^{12}C_3H_4O_2$
115.02	115.03	339.33	13.98	$^{13}C_2{}^{12}C$ methylglyoxal[M+H$_2$O+Na]	$^{13}C_2{}^{12}CH_4O_2$
119.07	119.00	181.89	7.49	$^{13}C_2{}^{12}C$ methylglyoxal [M+2Na-H]	$^{13}C_2{}^{12}C\ H_4O_2$
120.05	120.00	1339.32	55.18	$^{13}C_3$ methylglyoxal [M+2Na-H]	$^{13}C_3H_4O_2$

As formate was not detected by mass spectrometry due to its low concentration and molecular mass, we performed ^{13}C NMR on the labeled electrolyte sample and confirmed that ^{13}C was quantitatively incorporated into the formate product. This indicates that $H^{13}COO^-$ was also formed from either $^{13}CO_{2(aq)}$ or $H^{13}CO_3^-$. Because of the sample's high pH (9.82), furandiol and methylglyoxal underwent aldol condensation, forming oligomers that precipitated, and hence were not detectable by ^{13}C NMR of the solution.

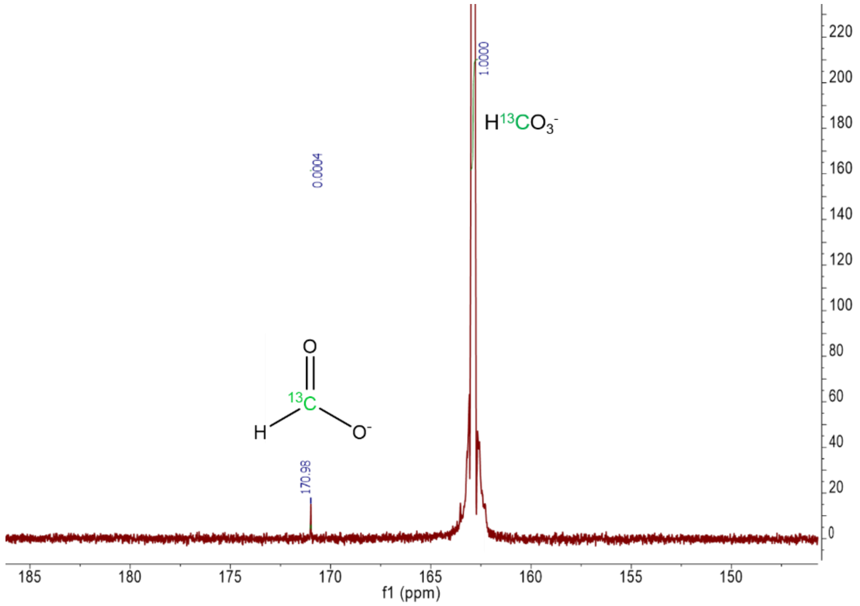

Figure 19: ^{13}C NMR of Ni_2P 0.00 V vs RHE electrolyte sample (plus 20% D_2O) with ^{13}C labeled bicarbonate. The 170.98 peak corresponds quantitatively to the formate/bicarbonate ratio expected from the HPLC experiments, showing that $HCOO^-$ is formed from the reduction of CO_2 or HCO_3^-. The spectrum was acquired with a Varian VNMRS 500 MHz, using decoupled-NOE 10000 scans at room temperature, with 3s relaxation delay.

16. Correlation between CO_2RR current density and phosphorus content

Figure S20 shows the linear relationship between the sum of the current density at all tested potentials with the phosphorus content of the catalyst, i.e. phosphorus rich compositions present an increased CO_2RR activity. While the precise determination of the role of phosphorus in the CO_2 reduction mechanism is beyond the scope of this paper, DFT calculations on Ni_2P and Ni_5P_4 show that phosphorus (rather than nickel) is the sitewith weak hydrogen adsorption[7]. Therefore, the overall higher activity of the phases with higher P content is consistent with the proposed mechanism, where three important steps involve reversible hydrogen transfer.

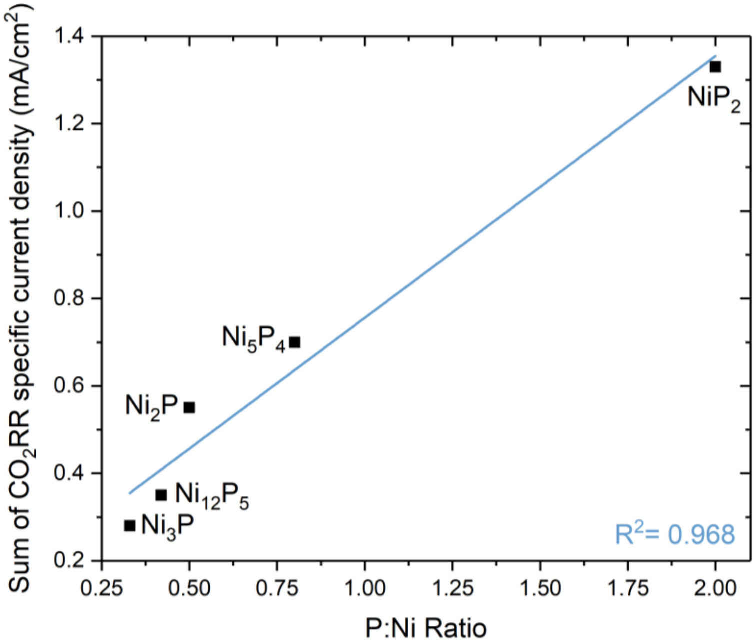

Figure S20: The sum of CO_2RR current density for all potentials depicted in the manuscript Fig. 4(A) is linearly correlated with the phosphorus content of the catalyst (P:Ni ratio)

17. Turnover Frequency Calculations

Turnover frequency (TOF) is defined by:

$$TOF = \frac{product\ formation\ rate\ (mol \cdot s^{-1})}{\#\ surface\ sites\ (mol)}$$

For the numerator, the product formation rate was measured using GC (for hydrogen) and HPLC (for formate, methylglyoxal and 2,3-furandiol) as described in Sections 7 and 10.
For the denominator, the number of surface sites, including nickel and phosphorus atoms, was estimated using the mehtod outlined below as the exact active site for the reaction is unknown.
First, the molar volume (V_m) of the compounds was calculated from its formula weight (F_w) and density (ρ):

$$V_m\left(\frac{cm^3}{mol}\right) = \frac{F_w}{\rho}\left(\frac{g \cdot mol^{-1}}{g \cdot cm^{-3}}\right)$$

The average surface occupancy was approximated using the equation below, where N_A is Avogadro's number:

$$Average\ surface\ occupancy\ (atoms \cdot cm^{-2}) = \left(\frac{\#\ atoms\ per\ formula\ unit \cdot N_A}{V_m}\right)^{\frac{2}{3}}$$

Finally, the number of surface sites was calculated using the product:

$$\#\ surface\ sites\ (mol) = \frac{Surface\ occupancy \cdot Roughness\ Factor \cdot Geometric\ Area}{N_A}$$

The geometric area is 3.14 cm^2 for all electrodes and the roughness factor is reported in Table S1.

Table S6: Values used to calculate the turnover frequency.

Catalyst	F_w **(g·mol^{-1})**	ρ **(g·cm^{-3})**	**Atoms per formula unit**	**Surface Occupancy (10^{15} atoms·cm^{-2})**	**Surface sites (µmol)**
Ni_3P	207.04	7.82	4	2.02	2.91
$Ni_{12}P_5$	859.13	7.54	17	2.01	1.65
Ni_2P	148.35	7.44	3	2.02	3.28
Ni_5P_4	417.33	6.32	9	1.89	2.11
NiP_2	120.63	4.57	3	1.67	3.04

18. Thermodynamic analysis of the CO_2 reduction mechanism

The table below contains the equilibrium potential for the reduction of $CO_2(g)$ to several organic compounds at pH 7, corresponding to the half-reaction:

$$mCO_2(g) + n(H^+ + e^-) \rightarrow C_aH_xO_y + oH_2O$$

The values reported here are calculated from the standard free energy of formation (ΔG_f^0) of the products and reactants, according to the equation:

$$E'^0 = [-1/nF] \cdot [\Delta_f G^0\ (product) - \Delta_f G^0(reactant)],$$

where *n* is the number of electrons added and *F* is Faraday's constant.

Table S7: Standard Gibbs free energy of formation ($\Delta_f G^0$) of reagents and common CO_2 reduction products and equilibrium potential of the CO_2RR half-reaction to that product. M, n, and o refer to the stoichiometric coefficients for CO_2, electrons/protons and water, respectively.

Compound	$\Delta_f G^0$ (kJ/mol)	Source	*m*	*n*	*o*	E'^0 (V vs RHE)
CO_2 (g)	-394.4	8				
H_2O (l)	-237.1	9				
OH^- (aq)	-229.99	8				
Carbon Monoxide (g)	-137.2	9	1	2	1	-0.10
Formate (aq)	-356.0	8	1	2	0	-0.02*
Formaldehyde (aq)	-129.7	8	1	4	1	-0.07
Glyoxal (l)	-189.7	9	2	6	2	-0.22
Methanol (aq)	-174.5	8	1	6	1	0.03
Acetate (aq)	-399.6	8	2	8	2	0.23*
Glycolaldehyde (l)	-288.7	10	2	8	2	-0.03
Methane (g)	-50.79	8	1	8	2	0.17
Acetaldehyde (l)	-127.6	9	2	10	3	0.05
Acetylene (g)	209.9	9	2	10	4	-0.05
Ethylene glycol	-508.6	9	2	10	2	0.20
Pyruvate (aq)	-352.0	9	3	10	3	0.04
2-hydroxy-2-propenal (l)	-212.9	11	3	12	4	0.02
Ethanol (aq)	-177.0	8	2	12	3	0.09
Ethylene (g)	68.4	9	2	12	4	0.08
Glyceraldehyde (l)	-442.2	10	3	12	3	-0.03
Methylglyoxal (l)	-253.96	10	3	12	4	0.02
2,3-Furandiol (l)	-400.99	11	4	14	5	0.01
Ethane (g)	-32.89	8	2	14	4	0.14
Hydroxyacetone (l)	-295.0	10	3	14	2	-0.31
Acetone (g)	-152.7	9	3	16	5	0.10
Allyl alcohol (l)	-92.0	10	3	16	5	0.06
Propionaldehyde (g)	-276.4	9	3	16	5	0.18
1-propanol (l)	-351.3	9	3	18	5	0.20
Propane (g)	-23.4	9	3	20	6	0.14

*Potential corrected for pH 7 by $E^0 + [(7 - pK_a) \cdot 0.059]$

Tabulated $\Delta_f G^0$ values of some products and reaction intermediates were not available. Thus, they were estimated using the individual group contributions method from Mavrovouniotis[10] and Jankowski[11]. In Table S8, the standard free energy of the CO_2 conversions is shown for every detected intermediate. After the endergonic reduction of CO_2 to formate and formaldehyde, the conversions to methylglyoxal and furandiol are exergonic at standard conditions.

Table S8: Standard Gibbs free energy ($\Delta_r G^0$) of the proposed reaction mechanism of CO_2 conversion to formic acid, methylglyoxal, and 2,3-furandiol.

Reaction	**$\Delta_r G^0$ (kJ/mol)**
$CO_2 + H^+ + 2e^- \rightarrow HCOO^-$	38.4
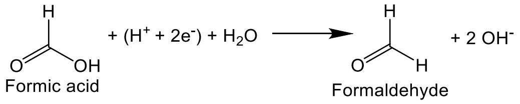	3.4
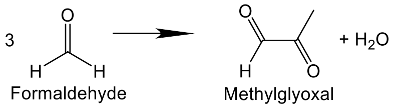	-102.0
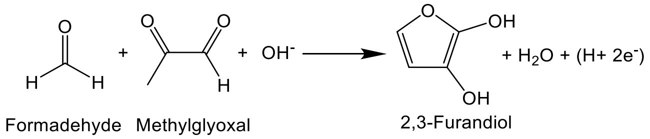	-24.4

19. Mechanism verification

The distinction between CO_2 and HCO_3^- as the source of carbon products is a major question in the CO_2 electroreduction field. While it is virtually impossible to isolate HCO_3^- and CO_2 because of the equilibrium between them in aqueous media we attempted to answer this question by using different buffers and purge gases for electrolysis that would result in different relative concentrations of the species of interest. Electrolysis was performed for 14 h at 0.00V vs RHE on Ni_2P.

$$H^+(aq) + HCO_3^-(aq) \rightleftarrows CO_2(aq) + H_2O(l)$$

The results summarized in Table S9 show that in very low concentrations of CO_2, using argon-purged bicarbonate solution, the selectivity of the reaction is very similar to CO_2-saturated HCO_3^-, however the amount of reduction products formed decreases from 53.0 µmol to 10.6 µmol. Conversely, in the absence of bicarbonate but constant purge of CO_2 in pyrophosphate buffer, the selectivity changes to favor hydrogen evolution and formate production, however the total amount of CO_2 converted is more than double of the CO_2-saturated $KHCO_3$. The electrolyte effect on enhancing HER is consistent with the good hydrogen donating ability and good buffering capacity of pyrophosphate. Together, these results indicate that the main source of carbon in aqueous CO_2, and that the bicarbonate ion acts as a "CO_2 buffer", suppling CO_2 through the equilibrium above, rather than being reduced itself in the ionic form. This observation is consistent with a recent report from Hursán and Janáky[12].

Table S9: Reduction of aqueous solutions with different concentrations of CO_2 and HCO_3^- on Ni_2P at 0.00 V vs RHE. Argon or CO_2 were purged at 5 sccm. The concentrations of CO_2 and HCO_3^- were estimated using Henry's Law and the equilibrium constant for the aqueous HCO_3^-/CO_2 equilibrium at room temperature and 1 atm. The influence of electrolyte concentration on CO_2 solubility was disregarded in the calculations, as these values are meant just for a rough comparison of species concentration. FE stands for Faradaic Efficiency, MG for methylglyoxal, and FD for furandiol.

	[$CO_{2(aq)}$] (mM)	**[HCO_3^-] mM**	**FE $HCOO^-$ (%)**	**FE MG (%)**	**FE FD (%)**	**Total CO_2RR FE (%)**	**$HCOO^-$ (µmol)**	**MD (µmol)**	**FD (µmol)**	**Total µmols of CO_2 con-verted**
CO_2-purged 0.5 M $KHCO_3$ (pH 7.5)	33	500	1.6	26.3	71.6	**99.5**	1.15	3.14	10.6	**53.0**
Ar-purged 0.5 M $KHCO_3$ (pH 9.8)	$1.6 \cdot 10^{-4}$	500	0.7	21.4	78.1	**100.2**	0.10	0.7	2.1	**10.6**
CO_2-purged 0.25M pyrophosphate buffer (pH 7.5)	33	0.12	3.8	10.2	13.3	**27.35**	20.5	13.6	14.4	**118.9**

Next, to verify the feasibility of the proposed mechanism (Figure 7 in the main text), sequential reduction of selected proposed intermediates was performed on Ni_2P at 0.00 V vs RHE for 14 h. The solutions containing a 25 mM concentration of the intermediate (formate, formaldehyde or methylglyoxal) and 0.25 M pyrophosphate buffer (pH 7.5) were continuously purged with argon to ensure that no dissolved oxygen or CO_2 remained in solution. Liquid products were quantified using

HPLC. The results are summarized on Table S10 below and show that formate and formaldehyde were reduced to methylglyoxal and furandiol. Both products were formed on a 1:1 ratio, a selectivity that mirrors the one observed when reducing CO_2 in the same buffer. Finally, methylglyoxal is also reduced to furandiol. While these results support the mechanism, further investigation using DFT is underway and will be necessary to fully elucidate the mechanism, define the catalyst active sites, and the relative energy of the catalyst-bound intermediates.

Table S10: Reduction of CO_2 and the proposed reaction intermediates formate, formaldehyde, and methylglyoxal to furandiol. The reactions were performed at 0.00 V vs RHE on Ni_2P.

Reagent and purge gas	**$HCOO^-$ produced (µmol)**	**Methylglyoxal produced (µmol)**	**Furandiol produced (µmol)**
CO_2-purged PPBS	20.5	13.6	14.4
Formate 25 mM (Ar-purged PPBS)	-	1.9	1.9
Formaldehyde 25mM (Ar-purged PPBS)	-	3.0	3.1
Methylglyoxal 25mM (Ar-purged PPBS)	-	-	1.6

20. Tafel Plots

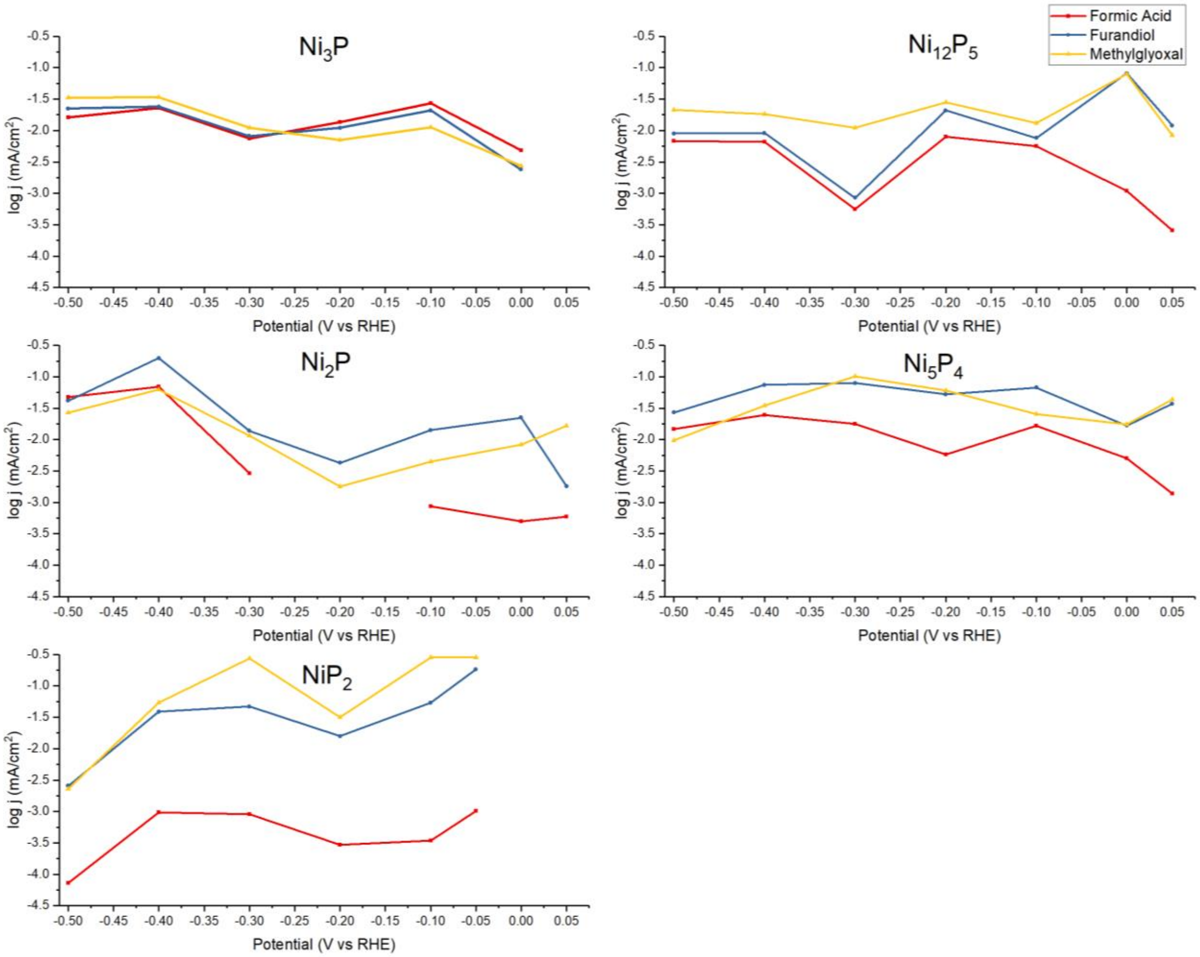

Figure S21: Tafel plots obtained by multiplying the faradaic efficiency for each product by the average current density at each potential.

21. Induction period

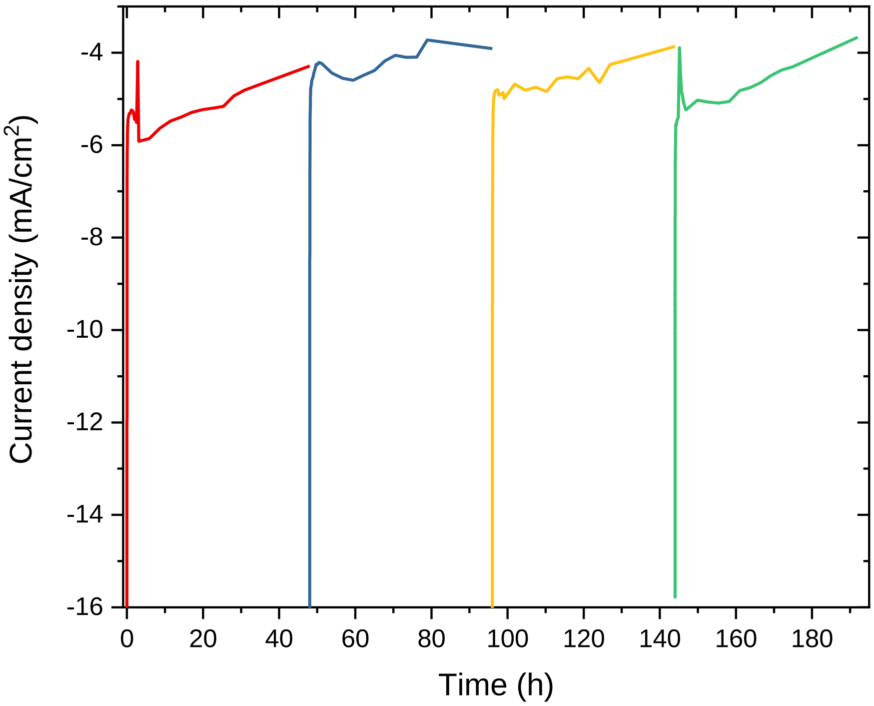

Figure S22: Four sequential 48-hour chronoamperometry traces at -0.5 V vs RHE on Ni_2P *in* CO_2*-saturated 0.5 M* $KHCO_3$*. Between each experiment, the cell and the catalyst pellet were rinsed and reused with fresh electrolyte. The initial break-in period with higher reductive currents is consistently observed and might indicate reactant/product gradient formation that is caused by the porous structure of the electrode.*

22. X-ray photoelectron spectroscopy

XPS analysis was performed on pristine electrodes (A-C) as well as after catalytic turnover (D-F). Here, catalytic turnover represents at least 3-4 full turnovers for CO_2RR per site as determined in the turnover frequency calculations. (A) is the detailed spectra of the C 1s and K 2p region, (B) is the detailed spectra of the Ni 2p region, (C) is the detailed spectra of the P 2p region, (D) is the detailed spectra of the C 1s and K 2p region, (E) is the detailed spectra of the Ni 2p region, and (F) is the detailed spectra of the P 2p region. Residuals are shown in **green** on the right y-axis using the same relative scale as the left y-axis.

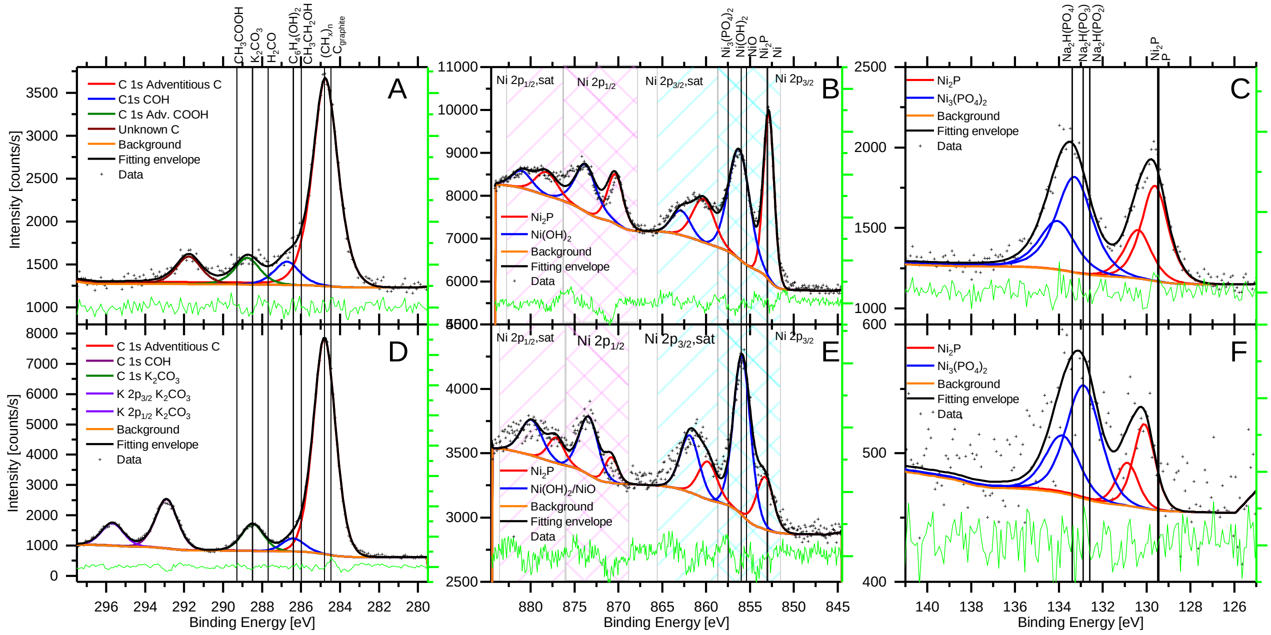

Figure S23 XPS of pristine (top) and post-reaction (bottom) Ni_3P

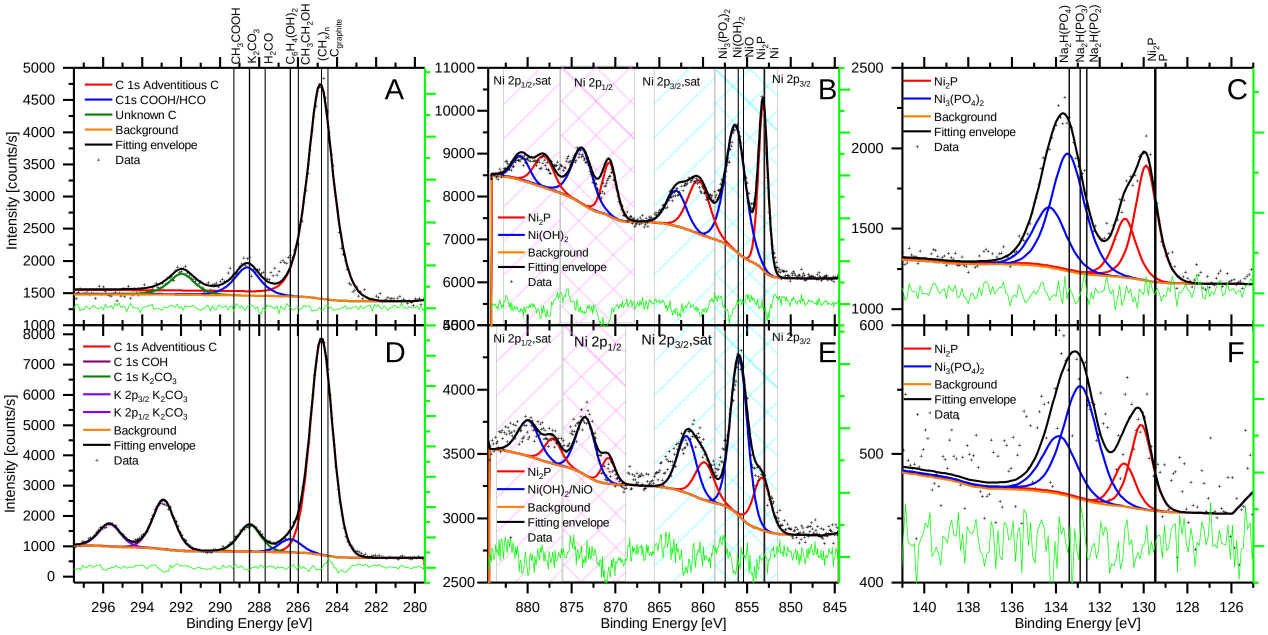

Figure S24: XPS of pristine (top) and post-reaction (bottom) Ni₁₂P₅

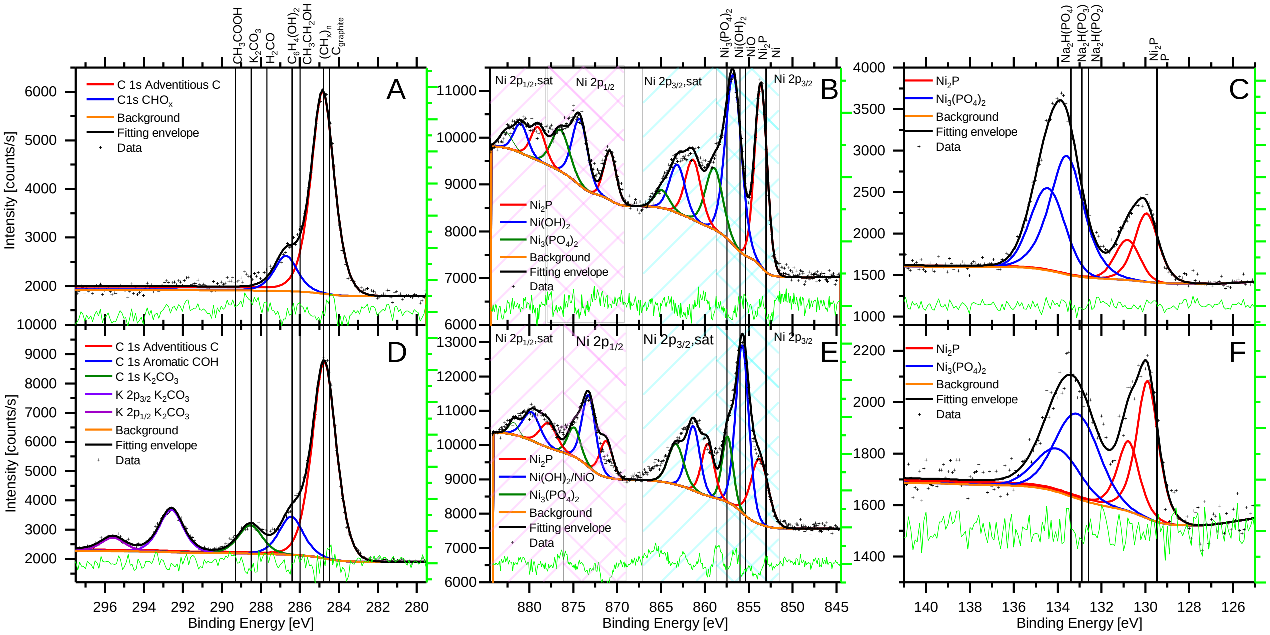

Figure 25: XPS of pristine (top) and post-reaction (bottom) Ni₂P

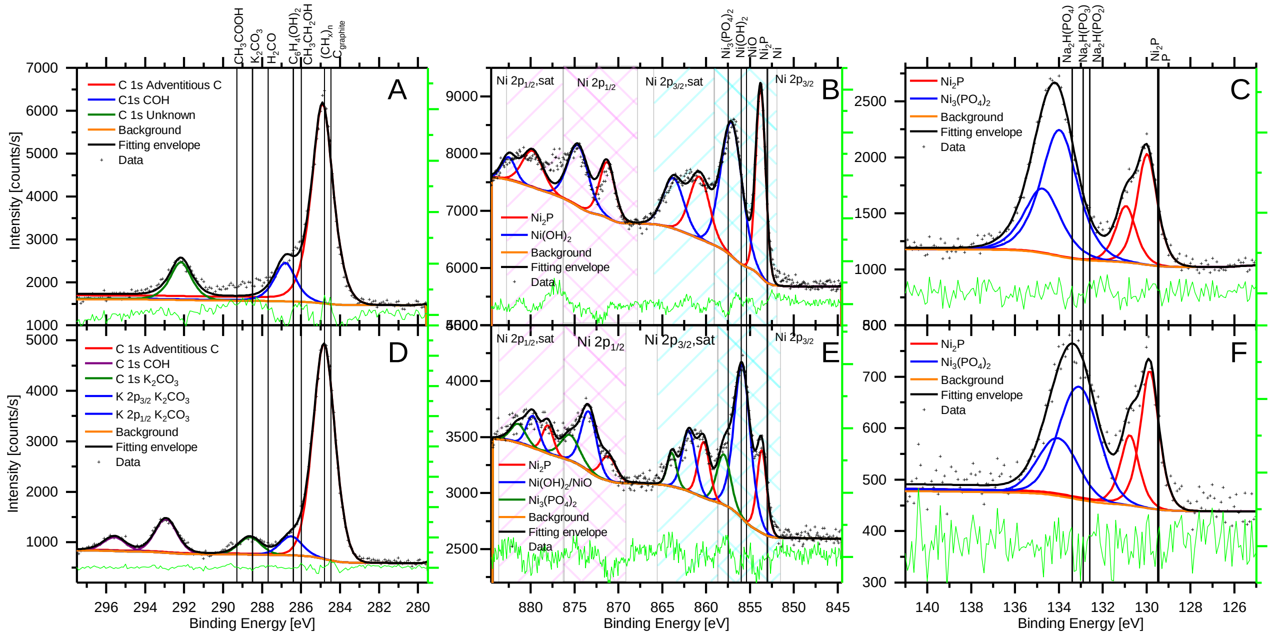

Figure S26: XPS of pristine (top) and post-reaction (bottom) XPS Ni_5P_4.

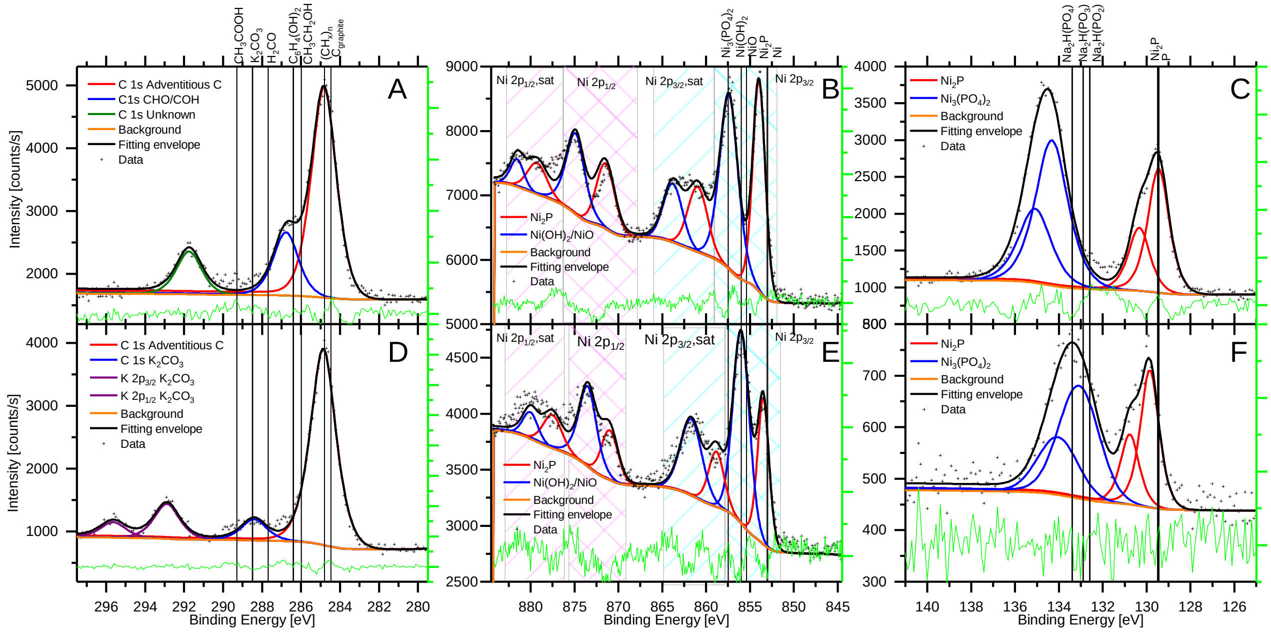

Figure S27: XPS of pristine (top) and post-reaction (bottom) NiP_2

23. Inductively Coupled Plasma Optical Emission Spectrometry (ICP-OES)

ICP-OES was conducted on a Perkin Elmer Optima 7300 DV to detect the amount of phosphorus and nickel that leached into the solution due to catalyst corrosion. The samples were prepared by diluting 500 µL of the post-reaction electrolyte with 2500 µL of 5% (v/v) nitric acid in ultrapure water. Immediately prior to sample analysis, a calibration was done with a serial dilution of a 100 ppm nickel and a 10 ppm phosphorus SPEX Certiprep certified analytical standards.

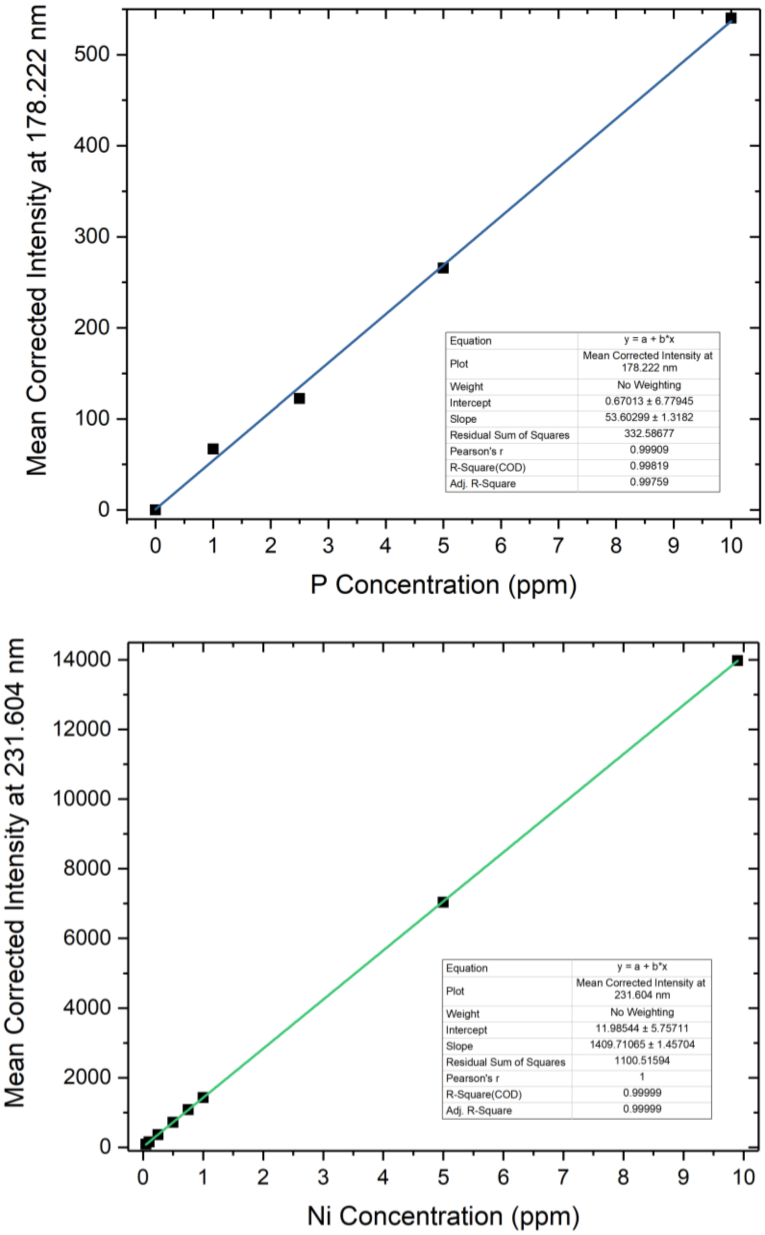

Equation	y = a + b*x
Plot	Mean Corrected Intensity at 178.222 nm
Weight	No Weighting
Intercept	0.67013 ± 6.77945
Slope	53.60299 ± 1.3182
Residual Sum of Squares	332.58677
Pearson's r	0.99909
R-Square(COD)	0.99819
Adj. R-Square	0.99759

Equation	y = a + b*x
Plot	Mean Corrected Intensity at 231.604 nm
Weight	No Weighting
Intercept	11.98544 ± 5.75711
Slope	1409.71065 ± 1.45704
Residual Sum of Squares	1100.51594
Pearson's r	1
R-Square(COD)	0.99999
Adj. R-Square	0.99999

Figure S28: ICP calibration curves for phosphorus (top) and nickel (bottom)

Table S11: Amount of nickel and phosphorus leached relative to the mass of catalyst on the cathode, after at least 3 hours of electrolysis, as measured by ICP-OES.

Catalyst	Potential (V vs RHE)	% Ni Leached	Standard Deviation	% P Leached	Standard Deviation
Ni_3P	0.05	0.001%	6.2E-07	0.025%	2.04E-05
	0.00	0.001%	3.8E-07	0.041%	1.48E-05
	-0.10	0.000%	3.0E-07	0.094%	2.85E-05
	-0.20	0.000%	1.3E-07	0.096%	1.54E-05
	-0.30	0.000%	0.0E+00	0.043%	2.02E-05
	-0.40	0.000%	2.5E-07	0.117%	2.58E-05
	-0.50	0.000%	5.4E-07	0.091%	1.89E-05
$Ni_{12}P_5$	0.05	0.002%	4.5E-07	0.114%	6.85E-06
	0.00	0.021%	7.2E-07	0.247%	8.89E-06
	-0.10	0.001%	3.3E-07	0.020%	2.82E-05
	-0.20	0.000%	3.0E-07	0.090%	1.42E-05
	-0.30	0.000%	4.8E-07	0.089%	6.23E-06
	-0.40	0.001%	4.0E-07	0.121%	1.76E-05
	-0.50	0.001%	3.4E-07	0.104%	1.89E-05
Ni_2P	0.05	0.000%	2.2E-07	0.058%	1.25E-05
	0.00	0.001%	3.6E-08	0.229%	2.38E-05
	-0.10	0.000%	3.8E-07	0.040%	1.98E-05
	-0.20	0.020%	1.1E-06	0.049%	5.13E-06
	-0.30	0.005%	2.8E-07	0.083%	8.60E-06
	-0.40	0.008%	4.7E-07	0.018%	1.90E-06
	-0.50	0.019%	1.1E-06	0.493%	5.13E-05
Ni_5P_4	0.05	0.005%	6.4E-07	0.199%	8.57E-06
	0.00	0.000%	8.9E-08	0.144%	4.88E-06
	-0.10	0.011%	5.4E-07	1.095%	6.57E-05
	-0.20	0.020%	1.4E-06	0.810%	3.08E-05
	-0.30	0.016%	2.0E-07	0.233%	1.86E-06
	-0.40	0.017%	5.6E-07	0.163%	1.47E-05
	-0.50	0.007%	8.0E-07	0.120%	6.83E-06
NiP_2	-0.05	0.003%	6.0E-07	0.147%	1.60E-05
	-0.10	0.023%	1.6E-06	1.010%	5.05E-05
	-0.20	0.003%	5.9E-07	0.255%	4.08E-06
	-0.30	0.005%	7.9E-07	0.312%	2.40E-05
	-0.40	0.009%	7.3E-07	0.136%	2.85E-06
	-0.50	0.002%	1.5E-06	0.053%	2.81E-06

24. References

1 J. Kibsgaard, C. Tsai, K. Chan, J. D. Benck, J. K. Nørskov, F. Abild-Pedersen and T. F. Jaramillo, *Energy Environ. Sci.*, 2015, **8**, 3022–3029.

2 I. Nemet, D. Vikić-Topić and L. Varga-Defterdarović, *Bioorg. Chem.*, 2004, **32**, 560–570.

3 A. M. Castillo, L. Patiny and J. Wist, *J. Magn. Reson.*, 2011, **209**, 123–130.

4 D. Banfi and L. Patiny, *Chim. Int. J. Chem.*, 2008, **62**, 280–281.

5 N. B. Bennette, J. F. Eng and G. C. Dismukes, *Anal. Chem.*, 2011, **83**, 3808–3816.

6 N. Sareen, E. L. Shapiro, A. N. Schwier and V. F. McNeill, *Atmos. Chem. Phys. Discuss.*, 2009, **9**, 15567–15594.

7 R. B. Wexler, J. M. P. Martirez and A. M. Rappe, *ACS Catal.*

8 A. J. Bard, R. Parsons and J. Jordan, *Standard Potentials in Aqueous Solutions*, International Union of Pure and Applied Chemistry, New York, NY, 1985.

9 D. R. Lide, *CRC Handbook of Chemistry and Physics*, CRC Press, 84th edn., 2004.

10 M. L. Mavrovouniotis, *J. Biol. Chem.*, 1991, **266**, 14440–14445.

11 M. D. Jankowski, C. S. Henry, L. J. Broadbelt and V. Hatzimanikatis, *Biophys. J.*, 2008, **95**, 1487–99.

12 D. Hursán and C. Janáky, *ACS Energy Lett.*, 2018, **3**, 722–723.